Journal of Mathematical Chemistry (2021) 59:364–404
https://doi.org/10.1007/s10910-020-01198-z

ORIGINAL PAPER

# Derivative NMR spectroscopy for J-coupled multiplet resonances using short time signals (0.5 KB) encoded at low magnetic field strengths (1.5T). Part I: water suppressed

**Dževad Belkić**[1,2] · **Karen Belkić**[1,2,3]

Received: 5 November 2020 / Accepted: 30 November 2020 / Published online: 22 December 2020


**Abstract**
The theme of this study is within the realm of basic nuclear magnetic resonance (NMR) spectroscopy. It relies upon the mathematics of signal processing for NMR in analytical chemistry and medical diagnostics. Our objective is to use the fast Padé transform (both derivative and nonderivative as well as parametric and nonparametric) to address the problem of multiplets from J-coupling appearing in total shape spectra as completely unresolved resonances. The challenge is exacerbated especially for short time signals (0.5 KB, no zero filling), encoded at a standard clinical scanner with the lowest magnetic field strengths (1.5T), as is the case in the present investigation. Water has partially been suppressed in the course of encoding. Nevertheless, the residual water content is still more than four times larger than the largest among the other resonances. This challenge is further sharpened by the following question: Can the J-coupled multiplets be resolved by an exclusive reliance upon shape estimation alone (nonparametric signal processing)? In this work, the mentioned parametric signal processing is employed only as a gold standard aimed at cross-validating the reconstructions from nonparametric estimations. A paradigm shift, the derivative NMR spectroscopy, is at play here through unprecedentedly parametrizing total shape spectra (i.e. solving the quantification problem) by sole shape estimators without fitting any envelope.

**Keywords** Derivative NMR Spectroscopy · Encoded short FIDs · J-coupling · Polyethylene phantom

✉ Dževad Belkić
Dzevad.Belkic@ki.se

[1] Department of Oncology-Pathology, Karolinska Institute, P.O. Box 260, SE-171 76 Stockholm, Sweden

[2] Medical Radiation Physics and Nuclear Medicine, Karolinska University Hospital, P.O. Box 260, 17176 Stockholm, Sweden

[3] School of Community and Global Health, Claremont Graduate University, Claremont, CA, USA

## 1 Introduction

### 1.1 The magnetic resonance principle and its experimental confirmation

Nuclear magnetic moments can very accurately be measured by the molecular beam method of Stern [1] from 1930. A modification called the molecular-beam resonance method of Rabi from 1938 has been used in the first successful demonstration of the magnetic resonance effect [2–4]. This detection is based on the magnetic resonance principle formulated by Groter [5] in 1936. It states that a precessing gyroscope can absorb energy from a periodic perturbation only if the precession frequency is equal (or nearly equal) to the frequency of the perturbation. Such a principle is universal, as besides nuclear magnetic moments, it applies equally well to any other system with angular momentum and magnetic moment.

A key feature of the nuclear magnetic resonance (NMR) spectroscopy is that the resonance frequency is proportional to the strength $B_0$ of the externally applied magnetic field[1]. Unlike modern spectrometers and clinical scanners, in the early years of NMR, the radiofrequency (RF) field was kept constant, whereas by changing the current, the strength $B_0$ of the main magnetic field was varied. In the measurement from Ref. [3], the RF field was about 3.5 MHz and the magnetic resonance was observed at $B_0 \approx 0.2$T through the trace of the absorption curve on the oscilloscope of the spectrometer.

In Ref. [3], a molecular beam (lithium chloride, LiCl) was first passed through a vacuum chamber before entering the magnetic apparatus. With such an arrangement, nuclei were practically isolated from each other as well as from their chemical environment. If all the further measurements continued in a like manner, solely with basically free nuclei, the NMR method, great as it is, would nevertheless remain to be an exclusively nuclear device tool, thus staying firmly within the boundaries of physics alone.

The situation changed dramatically in 1946 by the independent measurements of the two competing research groups led by Bloch [6–8] and Purcell [9, 10]. They demonstrated the existence of magnetic resonance in condensed matter using water and paraffin (containing protons), respectively. Such discoveries definitely crossed the borders of physics. These proofs of magnetic resonance in liquid and solid state matter paved the road for NMR physics first to other sciences and subsequently to technology and industry.

The "nuclear induction" method [6] and the "magnetic resonance absorption" method [9] are different, albeit they are both dealing with the same phenomenon, magnetic resonance. Bloch et al. [6] measured the current induced in a coil by reorientation of the bulk magnetization vector. On the other hand, absorption of the RF energy was the subject of measurement by Purcell et al. [9]. It is interesting to see

[1] The standard symbol for magnetic field strength is denoted by $H_0$, whereas $B_0$ labels magnetic induction. This distinction has been made in the older NMR literature. However, for a long time now, the NMR literature invariably denotes the magnetic field strength by $B_0$. Hereafter, we shall adhere to this latter convention, which has also been adopted in all conventional spectrometers and clinical scanners.

how the two competing terms coexisted in the early years. When finally Bloch and Purcell met, Bloch ("nuclear induction") adhered to Purcell's terminology ("nuclear magnetic resonance"). However, this stayed only within the realm of nomenclature.

Subsequently, the first commercial NMR spectrometer from 1952 (30 MHz, Varian Associates) and all its successors, including every clinical scanner (that came much later) implemented the method of Bloch [6] by encoding time signals or free induction decay (FID) curves. It was not an entirely unexpected choice given a close collaboration between Bloch's group and the Varian Associates (founded in 1948 by Russel Varian and Sigurd Varian in the Stanford Industrial Park, California). This choice of encoding, in fact, gave birth to NMR signal processing. If spectra continued to be directly measured and displayed on oscilloscopes or computer screens, any further resolution improvements could be achieved only by hardware upgrades (i.e. building stronger and much more expensive spectrometers to the benefit of fewer users). However, by encoding FIDs, these data, being stored in the computer memory, become readily accessible to analyses by a variety of signal processors. Some signal processors could extract more information from measured FIDs than any hardware upgrades. Hence, the importance of software upgrades, as well.

In the first encoding stage of FIDs, what is actually measured is the current induced in a coil surrounding a sample (spectrometers) or a part of a human body (clinical scanners). Afterwards, a discrete (equidistantly sampled) set of the FID data points is obtained from the encoded current by means of an analog-to-digital converter (ADC). Upon averaging many such encoded FIDs, the averaged time signal can be mapped from the time to the frequency domain by various mathematical transforms (Fourier, Padé,...) to yield the sought magnetic resonance (MR) spectrum. Thus far, surprisingly, all commercial NMR spectrometers and clinical scanners have built-in only the fast Fourier transform (FFT), a linear low-resolution signal processor with no ability to suppress noise from encoded FIDs.

### 1.2 Universal significance of chemical shift

Soon after Refs. [6, 9], there were further key measurements in NMR. Building upon the detection of the NMR phenomenon in bulk matter [6, 9], i.e. from nuclei in liquids and solids, new experiments [11–20] emerged with the most unexpected results. The surprise was in a dependence of resonance frequency on the chemical environment of nuclei. Such a resonance frequency displacement (or shift) is called chemical shift.

Chemical shifts have been measured not only in single compounds [11–19], but also in mixtures of molecules or chemical compounds [20]. The explanation was in electronic shielding of nuclei. Atomic and molecular electrons create a small, local magnetic field at the nucleus and this weakens the external static field $B_0$. As a result, the nucleus does not resonate at the anticipated Larmor frequency $\nu_L$ associated with $B_0$. Rather, it resonates at a smaller resonance frequency $\nu_R < \nu_L$, which is

associated with the difference between $B_0$ and the shielding magnetic field due to the electronic cloud about the nucleus[2].

It is important to refer explicitly to some of the specifics particularly from Refs. [13, 14]. Proctor and Yu [13, 14] measured the magnetic moments of several nuclei ($Mn^{55}$, $Co^{59}$, $Cl^{37}$, $N^{15}$ and $N^{14}$). In the case of the isotope $N^{14}$ of nitrogen, they used ammonium nitrate, $NH_4NO_3$. This choice has been made primarily because the sample $NH_4NO_3$ : (i) is highly soluble in water, $H_2O$, and (ii) has two nitrogens per molecule. Both factors (i) and (ii) were anticipated to enhance the intensity of the signal to be detected. However, the result was the observation of two different resonance frequencies. They were postulated to be one per group, the ammonium and nitrate ions, $NH_4^+$ and $NO_3^-$, respectively.

This assignment was confirmed by two separate measurements [14] using a pair of different samples, $NH_4C_2H_3O_2$ and $HNO_3$, each molecule having only one nitrogen. Here, they detected two different resonance frequencies, one for $NH_4C_2H_3O_2$ and the other for $HNO_3$, with the former and the latter being in close agreement with the respective resonance frequencies for $NH_4^+$ and $NO_3^-$ from $NH_4NO_3$. These findings cohere precisely with the said concept of chemical shift, implying that the local chemical surrounding of a spin-active nucleus changes its resonance frequency. As such, the two identical nitrogen nuclei are nonequivalent because they belong to two different groups ($NH_4$ and $NO_3$) of the same molecule ($NH_4NO_3$) [14].

The mentioned types of measurements on chemical shifts opened the door of an initially pure nuclear physics method, NMR, to e.g. chemistry for studying the structure of organic compounds (including macromolecules like proteins, lipids, fatty acids,...), elemental and isotope composition of various substances, etc.

### 1.3 Historic first NMR spectrum from measurements providing quantitative information: Ethanol

There seemed to be no dormant period in NMR since its inception. Thus, already in 1951, the opportunity for exporting NMR from physics to chemistry was seized by three physicists, Arnold, Dharmatti and Packard [21]. They furthered the finding of Proctor and Yu [13, 14] about nonequivalent behavior of identical nuclei in different groups of the same molecule. They made yet another key discovery, critically important quantitative information from spectra. One of their chemical compounds was ethanol ($CH_3CH_2OH$), a molecule with 3 sets of protons in 3 different groups, methyl ($CH_3$), methylene ($CH_2$) and hydroxyl (OH). The three protons from $CH_3$ are equivalent and so are the two protons from $CH_2$, viewed separately in their respective groups. On the other hand, the protons from $CH_3$, $CH_2$ and OH are all nonequivalent because they belong to three different groups. The oscilloscope linked to the

[2] In principle, the weak local magnetic field (say $\mathbf{b}_0$) at the nucleus generated by electrons can be parallel to the vector $\mathbf{B}_0$ or opposite to it, thus leading to an enhanced or reduced $B_0$, respectively. However, in most cases these two vectors ($\mathbf{B}_0$ and $\mathbf{b}_0$) are in the opposite directions, so that the term magnetic shielding is appropriate as it implies a reduced $B_0$ via $B_0 - \sigma < B_0$, where $\sigma > 0$ ($\sigma \equiv |\mathbf{b}_0|$).

spectrometer (0.76T) from Ref. [21] clearly showed 3 separate resonance peaks that the authors assigned to the 3 groups: $CH_3, CH_2$ and OH.

Such an assignment was made from the peak areas of the observed 3 resonances. These peak areas satisfied approximately the theoretically predicted relationships 3:2:1 for the resonance intensities associated with $CH_3, CH_2$ and OH, respectively. The latter ratios correspond to the numbers 3, 2 and 1 of nuclei in $CH_3, CH_2$ and OH, respectively. In this low-resolution spectrum of ethanol, with no fine structures, the peak areas are used because, as stated in Ref. [21], the peak widths found in the measurements were not equal for all the three detected resonances corresponding to $CH_3, CH_2$ and OH.

Overall, the work reported in Ref. [21] was historical because it was the first recorded NMR spectrum ever yielding quantitative information. Its significance cannot be understated as it implied that the resonance peak area gives the abundance of nuclei that contributed to the peak, i.e. to the magnetic resonance phenomenon. Hence a huge potential of NMR spectroscopy to identify not only different fragments of an examined molecule, but also the number of nuclei (per fragment) contributing to the given resonance peak.

### 1.4 Revisiting the problem of ethanol-containing spectra

Presently, we shall not address the ethanol problem [21] per se. Rather, ethanol will be the main molecule mixed with other molecules, notably methanol and acetate in a phantom provided by a manufacturer of MR clinical scanners (1.5T) [22, 23].

Use of phantoms is important for testing the performance of both clinical MR scanners and data analyzers (signal processors). A part of the quality control (QC) or the quality assurance (QA) programs is to test the reliability and reproducibility of encoding by using phantoms with the known amount (volumes, molar concentrations) of the given substances. With such a goal, a number of encodings of time signals for a phantom is performed over an extended period of time (e.g. 1–3 months) by medical physicists in hospitals. Each measurement would acquire about 100-200 FIDs for averaging to improve signal-to-noise ratio (SNR). This is usually referred to as the number of excitations (NEX). The latter nomenclature comes from the occurrence that a slice of a scanned object or tissue is externally excited by RF pulses. Time domain data averaging is necessary since all individual FIDs are too noisy to be useful for analysis and interpretation.

Manufacturers of MR scanners supply useful phantoms for NMR spectroscopy (NMRS), which is called magnetic resonance spectroscopy (MRS) in medicine[3]. For example, there is the General Electric (GE) brain phantom [24, 25] as well as the Philips "Phantom A" for proton MRS ($^1$H MRS) and "Phantom B" for phosphorus MRS ($^{31}$P MRS) [22, 23]. In conjunction with $^1$H MRS, which is the method of the present interest, we shall use the Phantom A (the Proton Phantom)

[3] The word "nuclear" is removed in medical applications of magnetic resonance to avoid the patient's potential fear from "nuclear radiation" which is, of course, not present in NMR.

filled with ethanol, methanol and acetate (alongside some other substances added to the mixture for technical purposes).

The GE brain phantom, a plastic sphere (16 cm diameter), is filled with several metabolites dissolved in a pH-buffered stock solution. These metabolites (also found in the gray matter of normal human brains in approximately similar amounts) are nitrogen acetyl aspartate (NAA), creatine (Cr), choline (Cho), glutamate (Glu), myo-inositol (m-Ins) and lactate (Lac) of molar concentrations 12.5, 10.0, 3.0, 12.5, 7.5 and 5.0 mM/L, respectively. For technical purposes also added are some other substances: potassium phosphate ($KH_2PO_4$, 50.0 mM), sodium hydroxide (NaOH, 5.0 mM) as well as 0.10% Azide (sodium azide) and 0.10% GdDPTA (Magnevest).

The polyethylene Philips Phantom A is of a special significance because it bears a close relationship with the mentioned first quantified spectrum in NMR history (the ethanol spectrum) from Ref. [21]. It is important to see how far this resemblance may go. Different resonances in a spectrum interact with each other. Therefore, it is intriguing to verify whether the presence of methanol and acetate in the said polyethylene mixture can notably influence the ethanol part of the whole spectrum.

The presently used FIDs have been encoded with water partially suppressed (by inversion recovery) at a 1.5T GE clinical scanner (Astrid Lindgren Children's Hospital, Stockholm). The residual water content is left intact for signal processing together with the other substances in the phantom. For encoding and signal processing employing the FIDs without water suppression during measurements, see our accompanying article [26].

The water-suppressed averaged FIDs are processed here by the nonderivative and derivative fast Padé transforms (FPT and dFPT), respectively, in both the parametric and nonparametric versions. Usually, even with the use of encoded water-suppressed FIDs, the resulting total shape spectra in virtually all shape estimators abound with overlapped resonances that offer no quantitative information. However, this situation with shape estimation has been dramatically changed by the introduction of the nonparametric derivative fast Padé transform, dFPT [27–31], the main focus of the present study.

Presently, we have a threefold goal. First, to see whether the overlapped peaks can be separated in nonparametrically reconstructed total shape spectra or envelopes. Second, staying still with nonparametric envelopes, to peer into the further, fine structure of ethanol, the triplet and quartet in the methyl and methylene group $CH_3$ and $CH_2$, respectively. The third goal, which is the most important, is to find out whether these J-coupled multiplets can unequivocally be resolved and accurately quantified exclusively by the low-order dFPT using only the nonparametric estimations of spectral envelope lineshapes.

Such a stringent benchmarking of signal processing is essential as it deals with measured time signals from chemical compounds containing molecules of known abundance. A successful performance of a signal processor in these testings is a prerequisite for applications to FID data encoded from substances of unknown content as well as to samples with the given mixture of chemical compounds, but with unknown concentrations of the individual constituents.

This kind of inverse problem is the workhorse of medicine viz: the effect is known and the cause is sought. It is also routinely practiced in engineering as "reverse engineering": performance of a given device is recorded. From the output data, the task is to reconstruct the input data with the underlying parameters. All of this is, by definition, the most salient signature of NMR spectroscopy in physics/chemistry and MRS in medical diagnostics [32–34].

## 2 Theory

This study on NMR spectroscopy is focused on nonderivative and derivative signal processings based on the nonparametric and parametric fast Padé transforms. These high-resolution estimations are well known and, as such, need not be presented here in full detail. Only the salient features will be briefly illuminated to guide the presentation and analysis in the Result Section. The Padé results will be compared with the corresponding Fourier findings to highlight their relative performance especially for derivative signal processing.

Time signals encoded from a sample, processed by the Padé methodologies, are represented quantum-mechanically by auto-correlation functions. These functions describe the time evolution of a general dissipative physical system or sample with $K$ constituents (metabolites in MRS). The system is governed by a dynamical non-hermitean operator ('Hamiltonian') and, thus, the frequency spectrum is comprised of complex eigenvalues (eigenenergies, eigenfrequencies). Most physical eigenfrequencies are nondegenerate. Nondegeneracy means that no two or more different eigenfrequencies can belong to the same eigenstate of the system. Degenerate spectra can equally well be treated by the fast Padé transform [29, 32, 33].

The auto-correlation function, or equivalently the time signal is given by a linear combination of $K$ fundamental complex harmonics $z_k$. Each harmonic function $z_k$ is a complex exponential $\exp(i\omega_k\tau)$ multiplied by a stationary complex amplitude $d_k$, where $\omega_k$ is the complex fundamental angular frequency (eigenfrequency) and $\tau$ is the constant sampling time (or dwell time):

$$c_n = \sum_{k=1}^{K} d_k z_k^n, \quad n \in [0, N-1], \quad z_k = \mathrm{e}^{i\omega_k\tau}, \quad \mathrm{Im}(\omega_k) > 0, \tag{2.1}$$

where $N$ is the total signal length. Here, $N$ is related to the total duration $T$ of the time signal by $T = N\tau$. Quantity $T$ is the total acquisition time in the measurement (encoding). The linear frequency $\nu_k$ is connected to $\omega_k$ by $\omega_k = 2\pi\nu_k$ (or generally, $\omega = 2\pi\nu$). The amplitude $d_k$ is the intensity of the $k$th component $z_k$ of the time signal, $d_k = |d_k|\exp(i\phi_k)$, where $\phi_k$ is the phase. Stated equivalently, $d_k$ is the complex-valued strength of the harmonic $z_k$.

The quantification problem, or equivalently, the spectral analysis problem, is an inverse problem with a specific name, the harmonic inversion (HI). It consists of reconstructing the unknown fundamental parameters $\{\nu_k, d_k\}$ $(1 \le k \le K)$ from the known time signal data points $\{c_n\}$ $(0 \le n \le N-1)$. The HI problem is linear in $d_k$ and nonlinear in $\nu_k$. Thus, determining both $\nu_k$ and $d_k$ amounts to solving a nonlinear

problem. Generally, nonlinear problems are not solvable exactly in any way. However, the HI problem can, in principle, be solved exactly (analytically for $1 \leq K \leq 4$ and numerically for $K \geq 5$) if each of the input data points $\{c_n\}$ is equidistantly sampled via $c(t) = c(t_n)$, where $t_n = n\tau$, as is customarily the case in NMRS and MRS.

The harmonics $\{z_k\}$ $(1 \leq k \leq K)$ represent damped trigonometric oscillations in the time domain. Their frequency domain counterparts in a nondegenerate spectrum are pure complex Lorentzian lineshapes. Each Lorentzian represents a component of the corresponding total shape spectrum. There are $K$ components in an envelope corresponding to $K$ harmonics in the time signal. For plotting, various modes of these complex spectra are used (e.g. magnitude as well as the real and imaginary parts). Such line profiles from spectra represent the response functions of the system to the external perturbations. In a physical system containing some degenerate eigenfrequencies, the corresponding spectral lineshapes are non-Lorentzians [32, 33].

The exact nonderivative quantum-mechanical spectrum in the frequency domain is defined by the finite-rank Green function as the MacLaurin polynomial [32, 33]:

$$S_N(z^{-1}) = \sum_{n=1}^{N-1} c_n z^{-n}, \quad z = \mathrm{e}^{i\omega\tau}. \tag{2.2}$$

For the given $S_N$, there are two variants of the fast Padé transform denoted by $\mathrm{FPT}^{(+)}$ or $\mathrm{FPT}^{(-)}$ that depend on the $z$ or $z^{-1}$, respectively. In the present study, only the $\mathrm{FPT}^{(-)}$ will be used and the fast Padé transform will be referred to simply as FPT.

For the given expansion (2.2), the nonparametric FPT is introduced by a ratio of two polynomials $P_{K'}/Q_K$ of generally different degrees ($K' \neq K$). In practice, the diagonal ($K' = K$) and paradiagonal ($K' = K - 1$) versions of the FPT are computationally most important due to their best (in the least-square sense) stability features of the expansion coefficients of the numerator ($P_{K'}$) and denominator ($Q_K$) polynomials [32]. We will presently adopt the diagonal FPT, in which case the total shape spectrum reads as:

$$\text{Nonparametric}: \quad \mathrm{FPT}_{\mathrm{Tot}} = \frac{P_K(z^{-1})}{Q_K(z^{-1})}, \tag{2.3}$$

where

$$P_K(z^{-1}) = \sum_{r=0}^{K} p_r z^{-r}, \quad Q_K(z^{-1}) = \sum_{s=0}^{K} q_s z^{-s}. \tag{2.4}$$

This version of the FPT is in the same variable $z^{-1}$ as in $S_N$. Therefore, the exact finite-rank Green function $S_N$ can be approximated by the FPT in the form $P_K(z^{-1})/Q_K(z^{-1})$ from (2.3) as:

$$S_N(z^{-1}) \approx \frac{P_K(z^{-1})}{Q_K(z^{-1})}. \tag{2.5}$$

The polynomial expansion coefficients $\{p_r, q_s\}$ in Eq. (2.4) are determined uniquely from the condition $S_N(z^{-1})Q_K(z^{-1}) = P_K(z^{-1})$ according to the defining relation (2.5) of the FPT:

$$\sum_{s=1}^{K} q_s c_{K+s'+s} = -c_{K+s'} \quad (1 \le s' \le N-K-1), \tag{2.6}$$

$$p_{r'} = \sum_{r=0}^{K} c_r q_{r'-r} \quad (0 \le r' \le K). \tag{2.7}$$

At first glance, there are two systems of linear equations to solve, one for $\{q_s\}$ and the other for $\{p_r\}$ in Eqs. (2.6) and (2.7), respectively. This is not the case, however, as actually only one system needs to be solved. Namely, after computing the coefficients $\{q_s\}$ of $Q_K$ by solving the single system in Eq. (2.6), the coefficients $\{p_r\}$ of $P_K$ become automatically available since Eq. (2.7) is then an analytical expression, the convolution of $\{c_n\}$ and $\{q_s\}$.

The Padé rational polynomial $P_K/Q_K$ is a complex total shape spectrum as a function of the sweep linear frequency $\nu$. This FPT is only a shape estimator. It is a nonparametric processor since it does not parametrize the spectrum, i.e. it does not autonomously generate the peak positions, widths, heights and phases.

To reconstruct the peak parameters, the FPT can alternatively be introduced as a parameter estimator. The starter of the procedure is the same envelope $P_K/Q_K$. This time, however, both $P_K$ and $Q_K$ polynomials are rooted. The roots of $P_K$ and $Q_K$ are the zeros and poles of the spectrum $P_K/Q_K$, respectively. This is true because the spectrum $P_K/Q_K$ is a meromorphic function. Meromorphic functions have poles as the only singularities. Polynomials $P_K$ and $Q_K$ have exactly $K$ roots each.

The parametric FPT first reconstructs the fundamental parameters $\{\omega_k, d_k\}$ of the time signal (2.1). Then, the $K$ component spectra are generated as the constituents of the envelope $P_K/Q_K$. The component shape spectrum $\mathrm{FPT}_{\mathrm{Comp}}$ of the $k$th resonance is the following complex Lorentzian (the $k$th partial fraction):

$$\text{Parametric}: \quad \mathrm{FPT}_{\mathrm{Comp}} = \frac{d_k z^{-1}}{z^{-1} - z_k^{-1}}. \tag{2.8}$$

The total shape spectrum $\mathrm{FPT}_{\mathrm{Tot}}$ is the sum of the $K$ component shape spectra, supplemented by a constant baseline. This is called the Heaviside partial fraction representation of $P_K/Q_K$ :

$$\text{Parametric}: \quad \mathrm{FPT}_{\mathrm{Tot}} = \frac{P_K(z^{-1})}{Q_K(z^{-1})} = \frac{p_0}{q_0} + \sum_{k=1}^{K} \frac{d_k z^{-1}}{z^{-1} - z_k^{-1}}. \tag{2.9}$$

The factored term $p_0/q_0$ is the baseline constant, which describes a flat background contribution to the spectrum $P_K/Q_K$. In Eqs. (2.8) and (2.9), quantity $z_k^{-1}$ is the $k$th nondegenerate root of the characteristic or secular equation $Q_K(z^{-1}) = 0$. This is the same fundamental harmonic from the time signal in Eq. (2.1).

Neither the $\mathrm{FPT}_{\mathrm{Comp}}$ nor the $\mathrm{FPT}_{\mathrm{Tot}}$ from Eqs. (2.8) and (2.9), respectively, is singular, i.e. they do not become infinite due to the inequality $z^{-1} \neq z_k^{-1}$. The sweep frequency $\nu$ in $z^{-1} = \exp(-2\pi i \nu \tau)$ is real, whereas the nodal frequency $\nu_k$ in $z_k^{-1} = \exp(-2\pi i \nu_k \tau)$ is complex, implying that indeed $z^{-1} \neq z_k^{-1}$.

Once the $k$th root $z_k^{-1}$ of $Q_K(z^{-1})$ becomes available, the fundamental frequency $\nu_k$ is deduced from the relation:

$$\nu_k = \frac{i}{2\pi\tau} \ln(z_k^{-1}). \tag{2.10}$$

Then the corresponding amplitude $d_k$ is obtained by using the Cauchy residue theorem. This gives $d_k$ as an analytical expression for the residue of the spectrum $P_K(z^{-1})/Q_K(z^{-1})$ taken at the eigenfrequency $z_k^{-1}$, so that:

$$d_k = \frac{P_K(z_k^{-1})}{Q'_K(z_k^{-1})}, \quad Q'_K(z^{-1}) = \frac{\mathrm{d}}{\mathrm{d}z^{-1}} Q_K(z^{-1}), \quad Q'_K(z^{-1}) \neq 0. \tag{2.11}$$

Both fundamental parameters $\nu_k$ and $d_k$ are complex, so that there are four real parameters per resonance, $\{\mathrm{Re}(\nu_k), \mathrm{Im}(\nu_k), |d_k|, \phi_k\}$, where $\phi_k$ is the amplitude phase, $d_k = |d_k| \exp(i\phi_k)$. The $k$th peak position and width are determined from $\mathrm{Re}(\nu_k)$ and $\mathrm{Im}(\nu_k)$, respectively. The $k$th Lorentzian peak height is proportional to the ratio of the magnitude $|d_k|$ of the FID amplitude $d_k$ and the imaginary nodal or characteristic frequency, $|d_k|/\mathrm{Im}(\nu_k)$. The $k$th peak phase is given by the FID amplitude phase, $\phi_k$. The peak area is the product of the peak height with the peak width. This implies that the peak area of a Lorentzian absorptive resonance is equal to $|d_k|/2$.

In MRS, metabolite concentrations are of key importance for diagnostics in radiology. Each such concentration is proportional to the given peak area, multiplied by a reference concentration (of an internal or external substance) for calibration purposes. Because the Lorentzian peak area is determined solely in terms of the FID magnitude $|d_k|$, it is tempting to think that the quantification HI problem, associated with the time signal (2.1), is linear (and, hence, much easier to solve) provided that the fundamental frequencies $\{\nu_k\}$ $(1 \leq k \leq K)$ are all known. This is, however, misleading and the HI problem remains nonlinear.

The reason is that while the chemical shifts, $\mathrm{Re}(\nu_k)$, might be known for many metabolites, the resonance widths, $\mathrm{Im}(\nu_k)$, are unknown. These widths are inversely proportional to the spin-spin relaxation times, $T_{2k}^{\star}$. It is the resonance width (or, more precisely, $T_{2k}^{\star}$), which must be known to properly correct the Lorentzian bare peak area ($|d_k|/2$) for the fact that, in practice, neither the total acquisition time ($T$) nor the so-called echo time (TE) is infinitely long [24].

A pole-zero coincidence can occur and it is called a Froissart doublet (the common roots to $P_K$ and $Q_K$) [35, 36]. The Froissart doublets describe noise or noise-like content (i.e. spuriousness) of the extracted information. Such coincidences lead to cancellations of $P_K$ by $Q_K$ in $P_K/Q_K$. This is known as pole-zero cancellation and it amounts to self-annihilation of Froissart doublets, in the original representation $P_K/Q_K$ of the Padé approximant. Such a cancellation becomes evident if $P_K/Q_K$ is written using the well-known canonical form for polynomials $P_K$ and $Q_K$ [35]:

$$\frac{P_K(z^{-1})}{Q_K(z^{-1})} = \frac{p_K}{q_K} \frac{\prod_{r=1}^{K}(z^{-1} - z_{r,P}^{-1})}{\prod_{s=1}^{K}(z^{-1} - z_{s,Q}^{-1})}. \tag{2.12}$$

Here, $z_{k,P}^{-1}$ and $z_{k,Q}^{-1}$ are the roots of polynomials $P_K(z^{-1})$ and $Q_K(z^{-1})$, respectively. Note that the root $z_k^{-1}$ of $Q_K(z^{-1})$ from Eqs. (2.1), (2.10) and (2.12), is relabeled as $z_{k,Q}^{-1}$ in (2.12).

The canonical representation (2.12) of the FPT permits yet another analytical expression for the amplitude $d_k$ as the residue of $P_K/Q_K$ from Eq. (2.12) taken at $z^{-1} = z_{k,Q}^{-1}$ :

$$d_k = \frac{p_K}{q_K} \frac{\prod_{r=1}^{K}(z_{k,Q}^{-1} - z_{r,P}^{-1})}{\prod_{s=1,s\neq k}^{K}(z_{k,Q}^{-1} - z_{s,Q}^{-1})}. \tag{2.13}$$

Froissart doublets are also washed out from the partial fraction representation (2.9) on account of the relations $d_k = 0$ (noise-free FIDs) or $d_k \approx 0$ (noise-corrupted FIDs). This is evident from Eq. (2.11), where $d_k = 0$ because $P_K(z_{k,Q}^{-1}) = 0$ for a Froissart doublet. Likewise, in Eq. (2.13), we have $d_k = 0$ since, by definition, $z_{k,Q}^{-1} = z_{k,P}^{-1}$ (pole-zero coincidence) for a Froissart doublet.

The weakness of Froissart doublets (through negligible small amplitudes $d_k$) is due to the fact that these resonances are associated with noise which is random. Any change significantly disturbs Froissart doublets and, as a result, they wobble in the complex frequency plane (e.g. with even the slightest truncation of the signal length $N$). This is how the noisy part of the reconstructed information is first reliably identified and then suppressed in the FPT. The underlying procedure is called the denoising Froissart filter (DFF) within the concept known as signal-noise separation (SNS) [35, 36].

Parameter $K$, as the common degree of polynomials $P_K$ and $Q_K$, is called the model order. Physically, it represents the total number of resonances in the spectrum $P_K/Q_K$. This number is unknown prior to signal processing. Numerical computations start with an initial value $K_{\text{in}}$, which is systematically increased until convergence has been reached as a function of $K$. In the parametric FPT, the signature of convergence is stabilization of the fundamental parameters $\{\nu_k, d_k\}$ with increasing $K$.

In the nonparametric FPT, stabilization of the entire spectrum $P_K/Q_K$ (within the chosen frequency interval) is the main criterion for selecting the physical (genuine) value $K_{\text{G}}$ of the running model order, starting with $K_{\text{in}}$, using a fixed step or increment $\Delta K$ $(K_{\text{in}} + \Delta K, K_{\text{in}} + 2\Delta K, \ldots, K_{\text{G}}, K_{\text{G}} + \Delta K, K_{\text{G}} + 2\Delta K, \ldots)$. Here, the DFF stabilizes the Padé spectrum $P_K/Q_K$ through pole-zero cancellations that filter out all the additional model orders beyond $K_{\text{G}}$ :

$$\frac{P_{K_G}}{Q_{K_G}} = \frac{P_{K_G+\Delta K}}{Q_{K_G+\Delta K}} = \frac{P_{K_G+2\Delta K}}{Q_{K_G+2\Delta K}} = \cdots = \frac{P_{K_G+L}}{Q_{K_G+L}} \quad (L > K_G). \tag{2.14}$$

Thus far, we discussed the nonderivative FPT. The expressions for spectra in the derivative fast Padé transform, dFPT, are obtained in their analytical forms by applying the general $m$th order derivative operator $D_m = (d/d\nu)^m$ $(m = 1, 2, 3, ...)$ to Eq. (2.5) and (2.9).

On the other hand, being limited always to shape estimations alone, Fourier signal processing begins by first defining the finite Fourier integral for the input continuous time function $c(t)$ as:

$$F = \frac{1}{T}\int_0^T dt e^{-2\pi i\nu t} c(t). \tag{2.15}$$

Subsequently, by discretizing the analogue time signal $c(t)$ via $c(t) = c(t_n) \equiv c_n$, where $t_n = n\tau$ $(0 \le n \le N-1)$, the Fourier integral (2.15) is mapped into the discrete Fourier transform (DFT):

$$F_k = \frac{1}{N}\sum_{n=1}^{N-1} c_n W_k^n, \quad W_k = e^{-2\pi ik/N}, \quad k \in [0, N-1]. \tag{2.16}$$

Finally, the DFT is expediently computed using the Cooley-Tukey $N\log_2 N$ algorithm (for $N = 2^\ell$, $\ell = 1, 2, 3, ...$) which is the nonderivative fast Fourier transform, FFT [32]. Here, resolution on the angular and linear frequency scale is given by the Fourier grid points, $2\pi/T$ and $1/T$, respectively. In other words, the resolving power in the FFT is the same for all time signals with the same duration $T$. Thus, the Fourier processing does not take into account the specific structure of a particular time signal under study. Moreover, the FFT considers all time signals as periodic, which is untrue in most cases of practical interest.

The derivative Fourier integral is introduced by subjecting Eq. (2.15) to the operator $D_m$ leading to:

$$D_m F = \frac{1}{T}\int_0^T dt e^{-2\pi i\nu t}\{(-2\pi it)^m c(t)\}. \tag{2.17}$$

In the derivative DFT, i.e. dDFT, the term $(-2\pi it)^m c(t)$ is discretized as $(-2\pi in\tau)^m c_n$. Thus, the dDFT is defined by:

$$F_k^{(m)} = \frac{1}{N}\sum_{n=1}^{N-1}\{(-2\pi in\tau)^m c_n\} W_k^n, \quad k \in [0, N-1]. \tag{2.18}$$

The dFFT is obtained by computing the dDFT by means of the Cooley-Tukey fast computational algorithm. In other words, the dFFT is generated by subjecting the modified time signal $\{(-2\pi in\tau)^m c_n\}$ to the nonderivative FFT. However,

the time-dependent power function $(-2\pi in\tau)^m$, as a weighting factor, emphasizes strongly the tail of the time signal. This is a huge disadvantage when applying the dFFT to encoded time signals because their tails contain mainly noise. Thus, the higher-order dFFT is basically processing noise alone and this leads to loss of all physical information [27]. This never happens in the dFPT due to the entirely different mathematical structure of the nonparametric and parametric derivative fast Padé transforms.

## 3 Results and discussion

First, subsection 3.1 addresses the phantom specifications and time-domain data acquisition. This is followed by subsection 3.2, which gives the salient features of the J-splitting pattern of resonances relevant to the phantom under study. Finally, subsection 3.3 is on reconstructions of spectra in the two modes, the real part of a complex spectrum and its magnitude.

### 3.1 Phantom content and time signal acquisition

We use the polyethylene Phantom A or Proton Phantom [22, 23]. It is a plastic sphere (10 cm diameter) filled with a mixture of ethanol (ethyl alcohol, EtOH, $CH_3CH_2OH$, 80%, 10 ml), acetate (acetic acid, Ace, $CH_3COOH$, 98%, 5 ml), methanol (methyl alcohol, MeOH, $CH_3OH$) and demineralized (demi) water ($H_2O$). For technical purposes, this phantom contains also phosphoric acid ($H_3PO_4$, 98%, 8 ml), 1 ml 1% arquad solution and copper sulfate ($CuSO_4$, 98%, 8 ml). The volumes of methanol and water are not stated in the Philips Manuals [22, 23].

In Refs. [22] (1989) and [23] (2014), two different chemical formulae for acetate are given, $CH_3OOH$ and $CH_3COOH$, respectively. The latter formula $CH_3COOH$ [23], will hereafter be used when referring to acetate (acetic acid), Ace.

Encoding by means of MRS used in the present work has been made with the described phantom using a 1.5T GE clinical scanner (Larmor frequency $\nu_L = 63.87$ MHz). It proceeded by employing single-voxel proton spectroscopy with the point-resolved spectroscopy sequence (PRESS) [24].

The encoding specifics of time signals or FIDs are: total signal length $N = 512$, echo time TE = 272 ms, repetition time TR = 2000 ms, bandwidth BW = 1000 Hz, sampling time $\tau = 1/\text{BW} = 1$ ms, total duration of each time signal $T = N\tau = 512$ ms and number of excitations (i.e. number of individual FIDs) NEX = 128. The acquired 128 FIDs are averaged. The averaged FID is subjected to Padé and Fourier estimations of total shape spectra by employing the nonderivative and derivative processings.

### 3.2 The pattern of J-splitting (spin-spin interaction)

Given the content of the polyethylene Phantom A, its absorption spectrum should display, according to the NMR theory, ten peaks: one for water, seven for ethanol (a

triplet plus a quartet), one for methanol and one for acetate. As discussed, a low-resolution spectrum of ethanol itself should have only three peaks as singlets associated with methyl, methylene and hydroxyl groups $CH_3$, $CH_2$ and OH, respectively. The OH peak is located near the water peak, which we presently place at 4.87 ppm (parts per million), corresponding to 20ºC [24]. For a large water concentration in the phantom, the hydroxyl OH peak (the smallest in the ethanol molecule) is swamped by the intense $H_2O$ resonance and, thus, invisible in a spectral envelope. This is why we do not count the OH peak and the displayed graphs will mainly focus on the frequency window containing ethanol and acetate.

In the case of a higher resolution, the other two groups of ethanol, $CH_3$ (methyl) and $CH_2$ (methylene) should undergo the so-called J-splitting due to nuclear spin-spin interaction, as prescribed by the spin Hamiltonian of the system. As usual, the J-splitting is manifested in a spectrum through the emergence of various multiplets at different chemical shifts. In particular, methyl $CH_3$ and methylene $CH_2$ groups of ethanol $CH_3CH_2OH$ should exhibit triplet (t) and quartet (q) peaks, respectively. This follows the so-called "$n + 1$" rule.

To illustrate this rule, we give an example of a molecule having 2 groups A and B with the corresponding number of nonequivalent protons $n_A$ and $n_B$, respectively. Then the interaction of spins of protons from these two groups will cause splittings of the spectral profiles from A and B into the multiplets of $n_B + 1$ lines in A and $n_A + 1$ lines in B. In the case of ethanol's groups $CH_3$(A) and $CH_2$(B), there are $n_A = 3$ and $n_B = 2$ protons, respectively.

Therefore, the spin-spin interaction of 3 methyl protons in $CH_3$ and 2 methylene protons in $CH_2$ will lead to multiplets in both $CH_3$ and $CH_2$. Specifically, since the neighbor B ($CH_2$) of A ($CH_3$) has 2 protons ($n_B = 2$), the spectrum of $CH_3 \equiv$ A will have a triplet (three resonances, $n_B + 1 = 3$). Likewise, because the neighbor A ($CH_3$) of B ($CH_2$) has 3 protons ($n_A = 3$), the spectrum of $CH_2 \equiv$ B shall have a quartet (four resonances, $n_A + 1 = 4$). Moreover, the intensities of the underlying component peaks in the $CH_3$ and $CH_2$ group of ethanol are read off from the Pascal triangle with the proportion values 1:2:1 and 1:3:3:1, respectively.

These latter relations can be explained as follows. The proportions 1:2:1 and 1:3:3:1 correspond to the binomial coefficients of 2 and 3, respectively. These binomial coefficients are the numbers in which each of the eigenvalues $m_s$ of the spin operator of the given group of ethanol can be found from the possible combinations of proton's spin quantum numbers $s = \pm 1/2$. For example, the eigenvalues $\{m_s = 0, \pm 1\}$ of the spin operator associated with the methyl group $CH_3$ can be found in 2 ways by combining the two spins $\pm 1/2$ of the protons. Similarly, $\{m_s = \pm 1/2, \pm 3/2\}$ of the spin operator corresponding to the methylene group $CH_2$ can be obtained in 3 ways by combining the two spins $\pm 1/2$ of the protons [37].

Thus, using higher resolution NMR spectroscopy, the spectrum of the polyethylene Phantom A should possess ten peaks (not counting the ethanol OH peak obscured by water) that are numbered in the Philips Manual [22] (p. 51) as:

- 1 (singlet, s): water ($H_2O$),
- 2-5 (quartet, q): methylene protons from the $CH_2$ group of ethanol (EtOH, $CH_3CH_2OH$),

- 6 (singlet, s): methanol (MeOH, $CH_3OH$),
- 7 (singlet, s): acetate or acetic acid (Ace, $CH_3COOH$) and
- 8-10 (triplet, t): methyl protons from the $CH_3$ group of ethanol (EtOH, $CH_3CH_2OH$).

### 3.3 Reconstruction of spectral envelopes

Both Padé and Fourier reconstructions can give spectral envelopes. As always, Fourier spectra appear only as total shape spectra. The same holds true for the nonparametric nonderivative FPT. However, the parametric FPT can provide the components and envelopes. The present spectral reconstructions are shown in 6 figures through a judicious combination of the Padé and Fourier output data:

- Figure 1: Padé, nonderivative FPT (nonparametric, no zero filling), real parts of complex spectra,
- Figure 2: Fourier, nonderivative FFT (no zero filling), real parts of complex spectra,
- Figure 3: Padé, nonderivative FPT and derivative dFPT (nonparametric, no zero filling) vs. Fourier, nonderivative FFT and derivative dFFT (no zero filling),
- Figure 4: Padé, nonderivative FPT and derivative dFPT (nonparametric, no zero filling) vs. Fourier, nonderivative FFT and derivative dFFT (FID zero filled once),
- Figure 5: Padé, nonderivative FPT and derivative dFPT (no zero filling); nonparametric (envelopes) vs. parametric (envelopes),
- Figure 6: Padé, nonderivative FPT and derivative dFPT (no zero filling); nonparametric (envelopes) vs. parametric (components).

We emphasize that, throughout the present work, all the Padé spectra are obtained using directly the encoded raw time signals with no zero filling and no preprocessing (e.g. no apodization, no filtering, ...). In testing convergence for Padé processing (parametric, nonparametric), the model order $K$ is varied until full convergence has been reached. All the present illustrations are made for the converged model order $K = 180$.

#### 3.3.1 Spectral envelopes by nonderivative shape estimators

Figure 1 shows the encoded average time signal and the nonparametric Padé reconstructions. The real (Re) and imaginary (Im) parts of the FID, $\{c_n\}$ $(0 \leq n \leq N-1, N = 512)$ are displayed on panels (a) and (d), respectively. The encoding specifics from subsection 3.1 are written on both panels, (a) and (d). No phase correction is made in the displayed $\mathrm{Re}(c_n)$ nor $\mathrm{Im}(c_n)$. The abscissae are either time (in units of the sampling time $\tau$) or the signal number $n$. The ordinates are in arbitrary units (au). Note that $\mathrm{Re}(c_n)$ and $\mathrm{Im}(c_n)$ are of comparable intensities on the ordinates from panels (a) and (d), respectively.

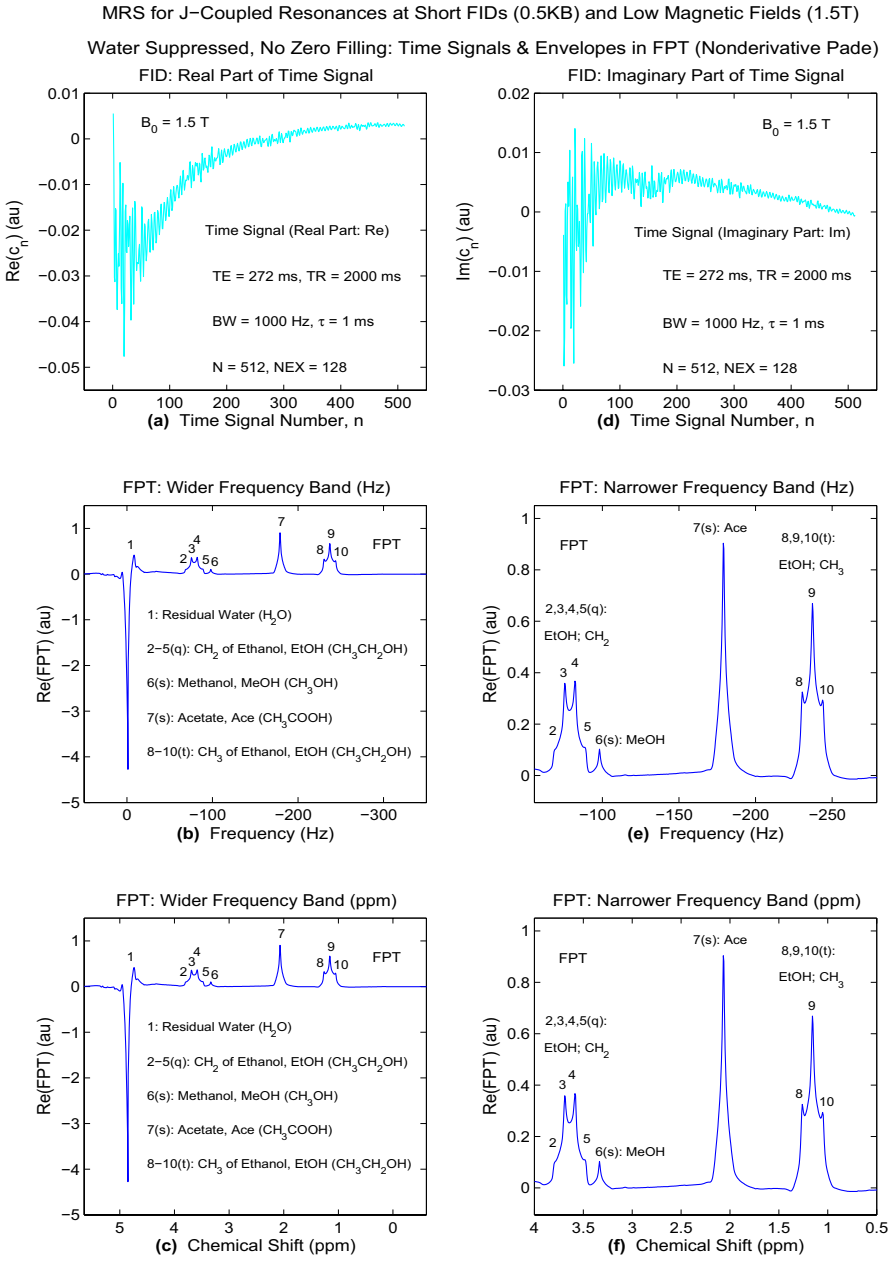


**Fig. 1** MRS for the standard Philips Phantom A [22, 23] with the main content: ethanol, methanol, acetate and water. Time signals or FIDs (**a**, **d**) of short length $N = 512$ encoded with water suppression at a 1.5T GE clinical scanner. No residual water suppression. Nonparametric Padé envelopes (**b**, **c**, **e**, **f**) with no zero filling of the FID. Wider (**b**, **c**) and narrower (**e**, **f**) frequency ranges. Spectral envelopes: abscissae in Hz (**b**, **e**) and ppm (**c**, **f**), ordinates in arbitrary units (au). For details, see the main text (Color figure online)

The real and imaginary parts of the FID are observed to take both positive and negative values. Water residual distorts the shape of the FID. We have not suppressed the remaining water content by processing nor in any other way. Because of its short length (only 0.5 kilobytes, KB)[4], this FID has not fully decayed in either its real nor imaginary parts on panels (a) and (d), respectively.

Panels (b), (c), (e) and (f) depict the real part $\{\mathrm{Re(FPT)} \equiv \mathrm{Re}(P_K/Q_K)\}$ of the complex Padé total shape spectrum $(P_K/Q_K)$ as intensities (ordinates in au) versus sweep linear frequencies (abscissae). The abscissae differ in two ways. One concerns the lengths of the frequency intervals (windows). The other relates to the units of frequency $\nu$. The left and right columns (b,c) and (e,f) show wider and narrower frequency windows, respectively. The second and the third rows (b,e) and (c,f) display the abscissae in hertz (Hz) and ppm, respectively. The former and the latter are dependent on and independent of $B_0$, respectively.

After encoding FIDs, clinical scanners show the real part (Re(FFT)) of the reconstructed complex Fourier spectrum as the computed intensities versus frequencies in Hz. This is the reason for showing panels (b) and (e) in Fig. 1. Otherwise, our entire analysis will be focused on the abscissae in ppm. The dimensionless units ppm for frequency are convenient as the locations of all the resonances remain unaltered by comparing the spectra computed from FIDs encoded or theoretically generated for different static magnetic field strengths $B_0$. Following a customary convention, all the numbers on the abscissae for frequency (both in Hz and ppm) are in the inverted order: from lower to higher values (upfield) when going from the right to the left (downfield is from left to right).

On panels (b) and (c) for a wider frequency interval, the residual (negative) water peak (#1) is dominant in the Padé envelope. It is pointed downward and lies mostly in the part of the plot associated with the negative values on the ordinate axis. The remaining resonances (##2 − 10) are oriented in the opposite direction and their lineshapes are mostly positive-definite. These resonances are seen to lie on a flat background baseline because the residual water does not have an elevated tail. This is a consequence of partially suppressing water in the course of encoding. The chemical names and formulae of the displayed resonances are written on panels (b) and (c) to facilitate the presentation.

The resonances ##2 − 10 of the main interest become more visible on a narrower frequency interval (avoiding water, #1) which is also shown in Hz (panel e) and ppm (panel f). Some of the expected resonances are clearly delineated, whereas the others are obscured to a varying degree. For example, both acetate, Ace, $CH_3COOH$ (#7) near 2.1 ppm and methanol, MeOH, $CH_3OH$ (#6) around 3.4 ppm are identifiable with certainty as the two isolated single resonances.

Moreover, the two groups of ethanol, EtOH, $CH_3CH_2OH$, that are methyl $CH_3$ near 1.3 ppm and methylene $CH_2$ close to 3.5 ppm, also exhibit their substructures in the Padé total shape spectrum on panels (e) and (f) in Fig. 1 pointing to the sought triplet and quartet resonances, respectively. Thus, from the expected triplet in the

[4] In information technology and particularly in the field of signal processing, including the present study, 1 kilobyte (KB) represents 1024 bytes.

$CH_3$ group, there is an evidently emerged middle peak (#9). The tops of the remaining two side peaks (##8,10) are clearly visible, as well. However, the remainders of these edge peaks (##8,10) are entirely glued to the tall resonance #9 from the $CH_3$ group of ethanol. The height of the middle peak #9 is about a factor of two taller that the tops of the shouldered peaks (##8,10). This may hint at an approximation to the exact ratios 1:2:1 only if the widths of all the peaks (##8,9,10) were the same, which is not known at this stage of the analysis. As discussed, a more appropriate estimate of the proportions 1:2:1 would be provided by the peak areas that, however, cannot be extracted even approximately from the overlapping resonances ##8–10.

As to the anticipated quartet from the methylene $CH_2$ group, the upper portions of the two middle peaks (##3,4) of the nearly same heights are clearly delineated on panel (f) for the Padé envelope. This is opposed to their immediate neighbors (the expected resonances ##2,5) in the $CH_2$ group that show up merely as two rough shoulders riding on the steep sides of the peaks #3 and #4, respectively. The heights of the middle peaks #3 and #4 are about 3 times larger than the tops of the shoulders #2 and #5, respectively. Recall that the corresponding exact ratios for the quartet in the $CH_2$ group is 1:3:3:1. Here, as mentioned, we do not address the hydroxyl OH group of ethanol (near the residual water placed at 4.87 ppm) because the location of the associated single peak is outside of the maximal frequency (4 ppm) considered in panel (f).

This discussion on the reconstruction results from Fig. 1 should be viewed in the light of the severe restrictions in the input data (short FID of 0.5 KB, no zero filling, encoding at a relatively weak $B_0 = 1.5$T). Given these limitations of the employed FID, the analyzed data in the output from the nonparametrically generated Padé total shape spectral profiles or envelopes from Fig. 1 can only be taken as qualitative. This particularly refers to the mentioned qualitative insights into the exact quantitative ratios 1:2:1 and 1:3:3:1 of the peak heights in the triplet and quartet resonances for the methyl $CH_3$ and methylene $CH_2$ groups of ethanol, respectively. Here, the adjective 'qualitative' refers to the circumstance that we provisionally relied solely upon the appearance of the peak heights in the plotted envelopes with no information about the peak widths. For unequal peak widths, it is inappropriate to use the peak heights for checking the proportions 1:2:1 and 1:3:3:1.

The ratio of the heights of e.g. the two given peaks could correspond to the ratio of the underlying resonating protons. This would be true only if the two peaks are of the identical widths. In the contrary case of the two unequal widths, instead of the peak height quotients, the correct number (abundance, concentration) of the resonating nuclei that generated the peaks should be obtained from the ratios of the corresponding peak areas. As discussed, this latter peak area procedure has been used in the first NMR spectrum of ethanol [21] to arrive at an approximate ratio 3:2:1 of the number of the resonating nuclei present under the three separate peaks due to methyl $CH_3$, methylene $CH_2$ and hydroxyl OH groups of $CH_3CH_2OH$ (no J-coupled resonances appeared in this low-resolution envelope).

Figure 2 is of the same type as Fig. 1, except that the Fourier envelopes are plotted this time. Also, the employed short FID ($N = 512$) is the same as in Fig. 1. For a wider frequency range in Hz on Fig. 2b, it is instructive to compare the present Fourier spectrum given by the real part Re(FFT)) with its counterpart from Fig. 4.13

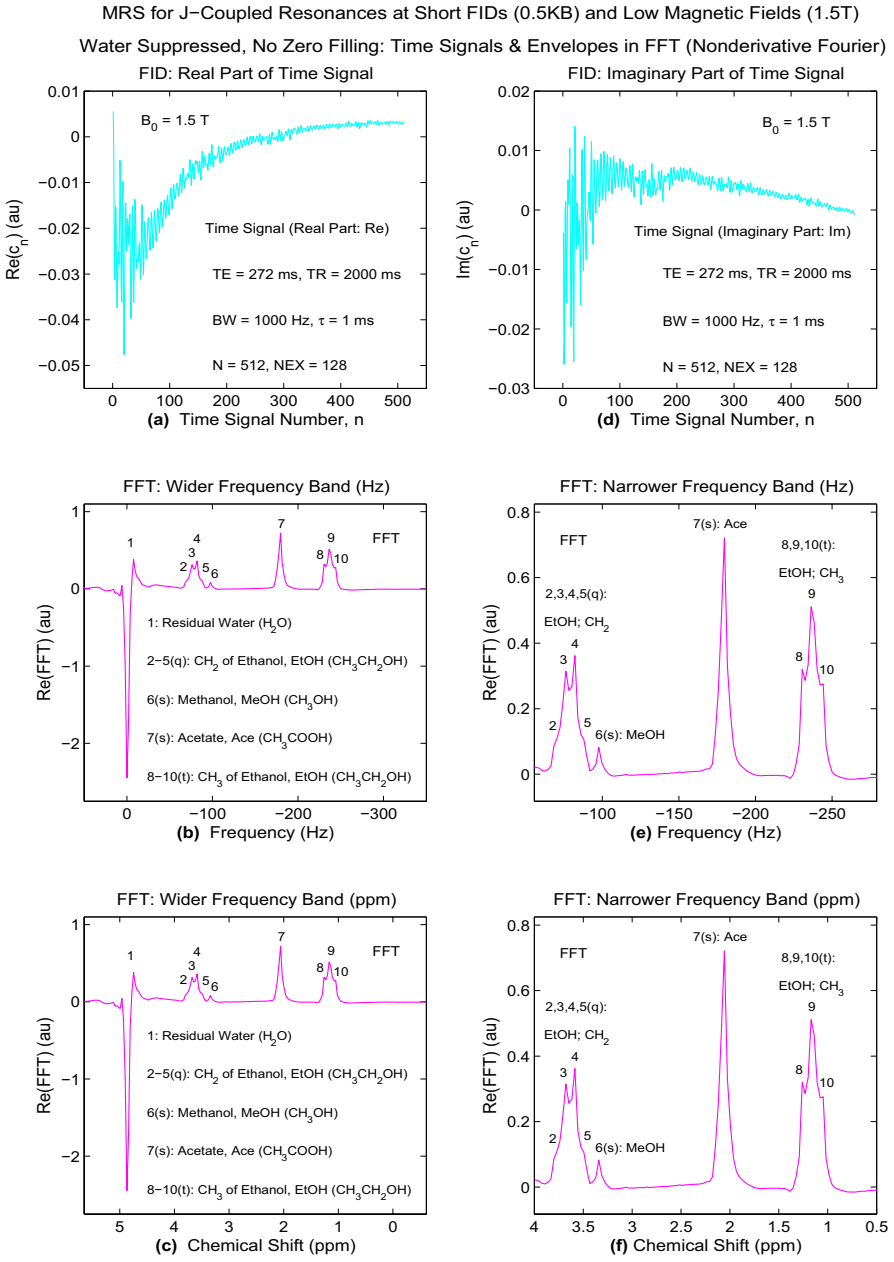


**Fig. 2** MRS for the standard Philips Phantom A [22, 23] with the main content: ethanol, methanol, acetate and water. Time signals or FIDs (**a**,**d**) of short length $N = 512$ encoded with water suppression at a 1.5T GE clinical scanner. No residual water suppression. Fourier envelopes (**b**, **c**, **e**, **f**) with no zero filling of the FID. Wider (**b**, **c**) and narrower (**e**, **f**) frequency ranges. Spectral envelopes: abscissae in Hz (**b**, **e**) and ppm (**c**, **f**), ordinates in arbitrary units (au). For details, see the main text (Color figure online)

in Philips Manual [22] (p. 82). In both cases, $B_0 = 1.5$T and the sweep frequencies cover the same interval $[-350, 50]$Hz. However, in Ref. [22], the signal length is eight times longer, including zero fillings ($N = 4096$: 1024 encoded FID data points plus 3072 zeros).

Still, this latter long FID gave the real part of the Fourier spectrum in Fig. 4.13 from Ref. [22] much of the same form as in our Fig. 2b. In other words, for the phantom under study, the use of merely 512 data points in the present FID does not impact adversely on the overall performance of the FFT. This is important to emphasize to avoid blaming the short signal length for any potential inadequacy that Fourier processing may face when the FFT complex spectrum is subjected to the derivative operator.

Given that Figs. 1 and 2 share the same theme, there is no need to repeat the whole discussion made about Fig. 1. Nevertheless, a few salient features of Fourier spectra should be singled out. This is worthwhile whenever there are some notable differences between the Fourier and Padé envelopes. First of all, comparing the spectra in Figs. 1 and 2, it is obvious that, as usual, the Fourier resolution is inferior to that of Padé.

Further, a few more particular features, can be summarized. For example, the negative water peak (# 1) in Fig. 2 appears not to descend as deeply as is the case in Fig. 1. The two ethanol groups, the methyl $CH_3$ ($\sim 1.25$ ppm) and the methylene $CH_2$ ($\sim 3.5$ ppm) protons, are seen on panel (f) of Fig. 2 as two amalgamated structures with no clearer hint on all the constituent individual peaks in the triplet and quartet resonances, respectively. Moreover, unlike the sharp appearance of the tops of the peaks #8 and #10 in the Padé spectrum in Fig. 1f for the methyl $CH_3$ ($\sim 1.25$ ppm) protons of ethanol, these two resonances are practically invisible in Fig. 2f. Therein, only 2 slight shoulders (##8,10) can barely be noticed on each side of the middle peak (#9), which is dominant in the $CH_3$ group.

Likewise, the hoped-for quartet (##2–5) in the methylene $CH_2$ group of ethanol is obscured in Fig. 2f. Here, the two middle resonances (##3,4) are of unequal intensity. This is opposed to the corresponding doublet of sharp resonances with nearly the same peak heights in the Padé envelope from Fig. 1f. Further, the peak heights of acetate (#7) and the $CH_3$ group of ethanol are significantly lower in the FFT (Fig. 2) relative to those in the FPT (Fig. 1).

Overall, some noticeable differences exist between the Padé (Fig. 1) and Fourier (Fig. 2) envelopes. Nevertheless, and this is most important, since they both stem from lineshape estimations alone, the farthest they can go on their own is to provide descriptions restricted to qualitative estimations at best. However, the ultimate goal of MRS is reconstruction of quantitative data. In the case under consideration, such quantitative data are the numbers of resonating protons that yield the given resonance.

The main question is: how can this goal be attained without fitting the spectral envelopes? One way is to go beyond shape estimation (nonparametric signal processing) as provided by parameter estimation from the onset. The latter estimation would give the peak parameters, four of them per peak (position, height, width, phase). The parametric FPT ranks high by its uniqueness, noise suppression (by way

of Froissart doublets, or equivalently, pole-zero cancellations) and exactness in solving the spectral analysis problem (the quantification problem) [32].

Nevertheless, we ask yet another essential question: would it be possible to perform full quantification of envelopes by using exclusively nonparametric processing for estimating spectral lineshape (with no fitting, of course)? Answering this question in the affirmative would erase the dividing line between the shape and parameter estimators. Guided by the questions of this fundamental type, the nonparametric derivative fast Padé transform, dFPT, has recently been introduced and implemented [27–31] to furnish a paradigm shift leading to derivative NMR spectroscopy (dNMRS) or derivative MRS (dMRS).

### 3.3.2 Derivative shape estimators: Padé versus Fourier

Derivative signal processing is the subject of Figs. 3–6. Among these, Figs. 3 and 4 compare the dFPT with dFFT. On the other hand, Figs. 5 and 6 deal with the dFPT alone. Figure 5 juxtaposes the two variants (nonparametric versus parametric) of the dFPT for total shape spectra. Finally, Fig. 6 provides the ultimately key information through comparisons of the envelopes from the nonparametric dFPT with the components from the parametric dFPT. The presently used derivative estimations of envelopes and components are concerned exclusively with the magnitude mode.

The real and imaginary parts, as two modes of an NMR complex spectrum, are inconvenient for the main theme of the present study, derivative signal processing. From our earlier investigation on derivative estimation of envelopes [27–29], it was seen that each resonance, in both the real and imaginary parts of the given complex derivative total shape spectrum, possesses its symmetric or nearly symmetric side lobes of wider widths than the breadth of the main, central peak. These side lobes (especially for higher derivatives) complicate extraction of the sought peak parameters from the real parts of complex derivative lineshapes. Such an obstacle is absent from the magnitude mode.

Generally, with an increase of derivative order, the peak width systematically diminishes and the peak height concomitantly augments [27–29]. Therefore, for derivative estimation in the magnitude mode, the side lobes (being wider than their parent central peak) become progressively smaller for higher derivatives and eventually are buried in the background baseline. In addition, side lobes are mitigated in the magnitude mode through combining the absorptive and dispersive parts of the given complex spectrum. Given these and other (e.g. phase-insensitiveness) significant advantages of magnitude envelopes, we opt to display derivative total shape spectra in the magnitude mode.

Usually, the magnitude spectral mode is not used in standard, nonderivative signal processing. The reason is in the fact that each peak in the magnitude envelope is wider by a factor of $\sqrt{3}$ relative to the width of the absorptive real part of the same complex Lorentzian spectrum. Moreover, the baseline is more elevated in a magnitude envelope than in the real part of the spectrum. However, the situation is completely different for derivative estimations using magnitude envelopes, particularly when the dFPT is utilized.

Most interestingly, e.g. the width of the given magnitude mode peak from the first derivative envelope is identical to that of the absorptive real part of the pertinent complex Lorentzian spectrum [29]. Even better, by taking further derivatives, the width of a magnitude derivative envelope becomes systematically further reduced.

In Figs. 3 and 4, comparisons are made between the FPT and FFT as well as between the dFPT and dFFT. For both figures, nonparametric Padé is used with no zero filling of the FID. In the case of Fourier processing, there is no zero filling either of the FID in Fig. 3. However, one zero padding of the time signal for Fourier estimations is made in Fig. 4. The left columns of Figs. 3 and 4 are for Fourier, whereas Padé refers to the right columns of these plots.

In Fig. 3, the nonderivative FFT on panel (a) appears to be of a notably lower resolution than the nonderivative FPT on panel (d). Returning to Fig. 1f, we recall that the real part of the Padé complex nonderivative spectral envelope shows several clearly delineated resonances. Such a situation is even more evident in the magnitude mode of the same Padé complex total shape spectrum in Fig. 3d. Interestingly, this occurs despite the fact that the peaks in the magnitude mode (Fig. 3d) are wider by a factor of $\sqrt{3}$ than their counterparts in the real part of the complex spectrum (Fig. 1f).

The reconstructions from the derivative estimations of spectra in the magnitude mode are shown on panels (b,c,e-j). Throughout, the derivative orders are relatively low: 1 (panel b: Fourier, e: Padé), 2 (c: Fourier, f: Padé), 3 (g: Fourier, h: Padé) and 4 (i: Fourier, j: Padé). The nomenclature for Padé and Fourier derivative envelopes in the magnitude mode are $|\mathrm{D}_m\mathrm{FPT}|$ and $|\mathrm{D}_m\mathrm{FFT}|$, respectively, where $\mathrm{D}_m$ is the $m$th order derivative operator with respect to the sweep linear frequency $\nu$, i.e. $\mathrm{D}_m = (\mathrm{d}/\mathrm{d}\nu)^m$ $(m = 1, 2, 3, ...)$.

Relative to the FFT (panel a), it is seen that the Fourier first derivative ($|\mathrm{D}_1\mathrm{FFT}|$, panel b) represents a considerable improvement. In contrast, the second derivative ($|\mathrm{D}_2\mathrm{FFT}|$, panel c) is visibly inferior to its predecessor $|\mathrm{D}_1\mathrm{FFT}|$ from panel (b). This deteriorating trend is exacerbated with the increased derivative order $m$. The tail of the water residual peak seen above 4 ppm on the Fourier panels (a), (b) and (c) eventually prevails at higher derivatives, thus making all the other resonances practically invisible. This amounts to a total breakdown of the dFFT for higher derivative orders.

The reason for this is the mathematical structure of the dFFT which processes the encoded time signal $\{c_n\}$ multiplied by the power function $(n\tau)^m$. The latter term, as per Eq. (2.18), puts emphasis on larger time signal numbers $n$ at which noise dominates the physical FID data points. Even for the derivative orders $m$ as low as 2 on panel (c), it is observed that the said mathematical feature of the dFFT is detrimental in any attempt to perform meaningful estimations by the derivative Fourier transform. Possibly, this could be mitigated somewhat by using an exponential apodizing function, i.e. multiplying $\{(n\tau)^m c_n\}$ by a decaying exponential. We have not made such an attempt as it is always better to process the originally encoded raw FIDs instead of their modifications via e.g. apodization and the like artificial devices. In any case, any exponential apodization would broaden the peaks, contradicting the main goal of derivative estimations: significant narrowing of the reconstructed spectral lines.

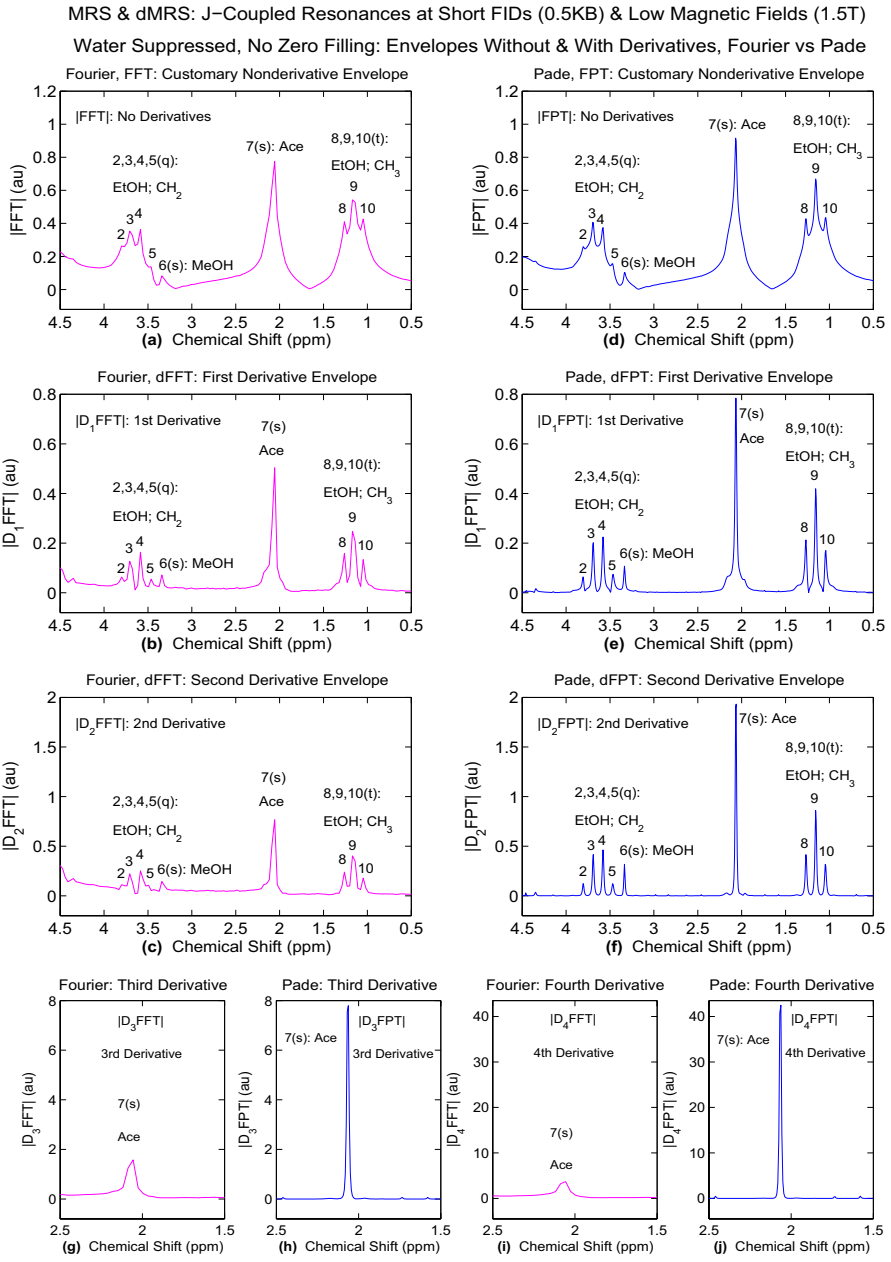


**Fig. 3** MRS and dMRS for the standard Philips Phantom A [22, 23] with the main content: ethanol, methanol, acetate and water. Processing of time signals of short length $N = 512$ encoded with water suppression at a 1.5T GE clinical scanner. No residual water suppression. Nonderivative and derivative envelopes with no zero filling for two processors: Fourier (**a**, **b**, **c**, **g**, **i**) and nonparametric Padé (**d**, **e**, **f**, **h**, **j**). Abscissae in ppm, ordinates in arbitrary units (au). For details, see the main text (Color figure online)

To proceed further, we turn our attention to the derivative Padé transform, dFPT, through $|D_m\text{FPT}|$ obtained with the intact encoded FID and shown on panels (e), (f), (h) and (j) for $m = 1, 2, 3$ and 4, respectively. Regarding all the peaks ##2–10, the first Padé derivative $|D_1\text{FPT}|$ (panel e) exhibits an astounding resolution improvement over |FPT| (panel d). In $|D_1\text{FPT}|$ from panel (e), these resonances are sharply pulled out from their irregular, low-lying lineshapes hidden in the baseline of |FPT| on panel (d). The prerequisite for the overall improvement of $|D_1\text{FPT}|$ (panel e) over |FPT| (panel d) is in having a tremendously flattened baseline, which is practically immersed into the abscissa. Moreover, the expected J-splittings in ethanol yielding the quartet and triplet in the $CH_2$ and $CH_3$ groups, respectively, are achieved already in $|D_1\text{FPT}|$ on panel (e).

Panel (f) shows the Padé second derivative, $|D_2\text{FPT}|$. Herein, several key advances are patently clear. Thus, regarding the quartet and triplet of ethanol, there is a significant resolution improvement when passing from $|D_1\text{FPT}|$ (panel e) to $|D_2\text{FPT}|$ (panel f). Here, the net gain by using $|D_2\text{FPT}|$ is in straightening up and symmetrizing the triplet and quartet of ethanol by suppressing the sidebands that are present in $|D_1\text{FPT}|$. All the nine peaks (##2–10) in the Padé second derivative magnitude spectrum on panel (f) are seen to be of the bell-shaped Lorentzian profiles. For acetate (#7), the low-lying shoulders in $|D_1\text{FPT}|$ (panel e) are suppressed in $|D_2\text{FPT}|$ (panel f). Herein, $|D_2\text{FPT}|$ exhibits two very small satellite peaks, symmetrically positioned on each side of the acetate peak (#7). However, they are not present in $|D_3\text{FPT}|$ nor in $|D_4\text{FPT}|$ shown on panels (h) and (j), respectively.

The abscissae in panels (g–j) are restricted to a small band around the acetate peak alone for a better visualization of the satellites under higher derivatives, $|D_m\text{FPT}|$ ($m = 3, 4$), on the scales of the displayed ordinates. This check was optional since, in fact, the entire estimation by the dFPT is finalized extremely fast, already through the second derivative $|D_2\text{FPT}|$ for all the nine resonances ($\#\#2 - 10$). For this reason, it is fully sufficient to complete the presentation of the dFPT with at most the second derivative for all the nine resonances (##2–10).

This offers an answer to the following working question: where do we stop in Padé derivative estimation (i.e. at which derivative order $m$)? As a rule of thumb, among a sequence of the employed $m$ values, the lowest derivative order $m = m_{\min}$ to be retained as the final result in the dFPT can safely be the one for which all the physical (genuine) resonances are fully resolved preferably to the level of a minimal background baseline. In the present study, this stopping criterion is optimally fulfilled for $m_{\min} = 2$, as per Fig. 3f.

The present short FID with only 512 encoded points, subjected to Fourier processing without zero filling of the time signal, yields merely 512 Fourier grid points in the frequency domain. That this is insufficient is obvious in Fig. 3 from panels (g) and (i) for $|D_3\text{FFT}|$ and $|D_4\text{FFT}|$, respectively. Therein, the heights of the acetate peaks from these two Fourier derivative envelopes are shortened because of having too sparse Fourier grid frequencies. To check whether zero filling would somewhat improve Fourier processing, we refer to Fig. 4. Also in this figure, no zero filling of the FID is made for Padé processing as this is unnecessary. Therefore, the Padé results for $|D_m\text{FPT}|$ ($m = 0 - 4$) on panels (d–f,h,j) of Figs. 3 and 4 are identical.

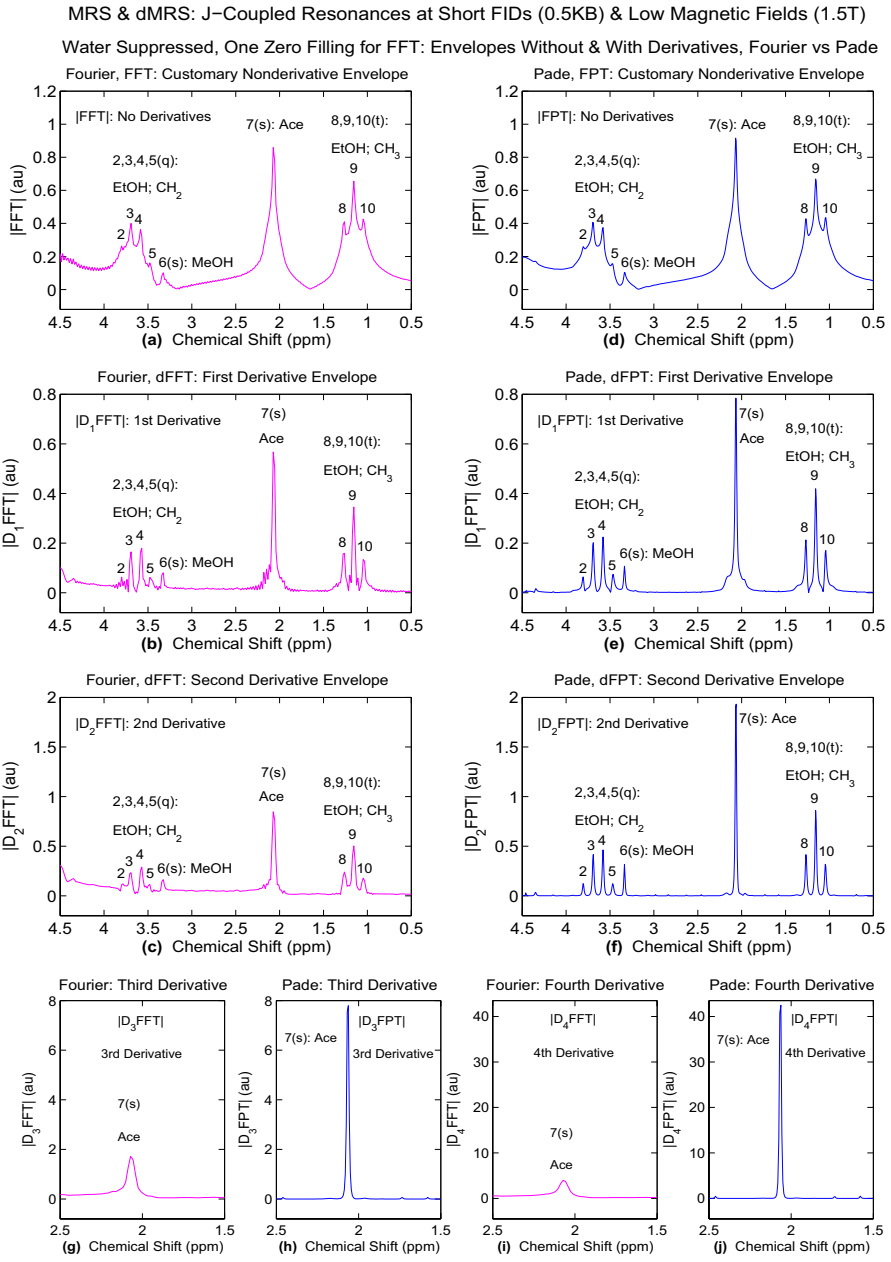


**Fig. 4** MRS and dMRS for the standard Philips Phantom A [22, 23] with the main content: ethanol, methanol, acetate and water. Processing of time signals of short length $N = 512$ encoded with water suppression at a 1.5T GE clinical scanner. No residual water suppression. Nonderivative and derivative envelopes: Fourier with one zero filling (**a**, **b**, **c**, **g**, **i**) and nonparametric Padé with no zero filling (**d**, **e**, **f**, **h**, **j**). Abscissae in ppm, ordinates in arbitrary units (au). For details, see the main text (Color figure online)

Zero filling in the time domain corresponds to a trigonometric interpolation in the frequency domain when using Fourier estimations. This yields more Fourier grid frequencies. However, the disadvantage is the appearance of spectral wiggles in Fourier envelopes as seen on panel (a) in Fig. 4 for the nonderivative processing. Such wiggles, stemming from an artificially elongated FID, evidently lead to distortions of Fourier envelopes.

Artifacts appearing as wiggles due to zero filling of the FID are seen to persist also in the first Fourier derivative, $|D_1FFT|$ (Fig. 4b). On the other hand, these wiggles are significantly diminished in $|D_2FFT|$, which has a slightly better appearance on Fig. 4c (one zero filling) than on Fig. 3c (no zero filling). There are no wiggles on panel (g) nor on panel (i) in Fig. 4 for $|D_3FFT|$ and $|D_4FFT|$, respectively. These two latter spectra (one zero filling) have slightly taller acetate peaks than their counterparts in $|D_3FFT|$ and $|D_4FFT|$ in Figs. 3g and 3i (no zero filling).

All told, the results of the nonderivative Fourier processing yielding |FFT| (one zero filling) in Fig. 4a is deteriorated (through the emergence of dense wiggle artifacts) relative to |FFT| from Fig. 3a (no zero filling). Moreover, according to Figs. 3b and 4b, the first Fourier derivative, $|D_1FFT|$, is not helped either by zero filling. Further, panels (c), (g) and (i) in Figs. 3 and 4 show that only the lineshapes of acetate in $|D_mFFT|$ ($m = 2, 3, 4$) are somewhat improved for the zero-filled FID relative to the case with no zero filling in the dFFT.

However, nothing of substance is gained for ethanol and methanol by zero filling of the encoded time signal in the Fourier estimation, supplemented by the derivative transform of orders $1 \leq m \leq 4$. Thus, it appears from Figs. 3 and 4 that, generally, zero filling is of no notable use in the dFFT, on top of impacting adversely on the corresponding nonderivative Fourier estimation, FFT. For $m > 4$ it is immaterial whether zero-filling is used or not since the dFFT fails flagrantly for higher derivatives.

We have not discussed Padé processing in Fig. 4 since this is already done when analyzing Fig. 3. Namely, as stated, these two figures use the same FID with no zero filling and thus show the same results for $|D_mFPT|$ ($m = 0 - 4$). The latter Padé results are replotted in Fig. 4 merely as the reference data that help the presentation of the Fourier reconstructions.

Overall, it is seen from Figs. 3 and 4 that the dFFT (without and with zero filling, respectively) is inappropriate for derivative estimations of total shape spectra. This is due to processing not the encoded input FID, $\{c_n\}$, but rather the product of the time signal with the power function $(n\tau)^m$. In other words, as per section 2, it is a weighted FID, namely $\{(n\tau)^m c_n\}$, which is subjected to the dFFT. The multiplier $(n\tau)^m$ stems from the application of the derivative operator $D_m = (d/dv)^m$ to the expression for the complex Fourier transform. The extra term $(n\tau)^m$ weighs much more the noisy part of the FID at its larger signal number $n$ than the earlier encoded data points. Worsening of processing by the dFFT relative to FFT, is reflected in lower resolution and SNR. This, in turn, broadens the spectral widths of resonances. Such deteriorating features of the dFFT are diametrically opposite to what is expected from properly designed derivative estimations.

In sharp contrast, however, the dFPT (which uses the intact encoded FID, $\{c_n\}$, with no zero filling) steadily keeps on providing the unprecedentedly improved

derivative estimations. This is achieved by the mechanism of a systematic narrowing of the widths of resonances and a concomitant increasing of the peak heights with augmented derivative order $m$. As a result of this synergistic roadmap, Padé derivative resonances are very sharp. Consequently, the overlapped peaks are split apart. This lowers the baseline levels, as per panels (d–f,h,j) in Figs. 3 or 4.

Viewed together, the almost fully suppressed background baselines and the larger peak heights lead to simultaneously improved resolution and SNR in the dFPT relative the dFFT. Further, while focusing on Padé-based shape estimations in Figs. 3 or 4, it is clear that such a twofold improvement is also achieved by the dFPT (derivative Padé, panel f) relative to the FPT (nonderivative Padé, panel d). This lends firm support to the nonparametric dFPT.

### 3.3.3 Derivative Padé processing of envelopes: nonparametric versus parametric estimations

Thus far, the focus was on shape estimations by means of Padé and Fourier nonparametric signal processings. The remaining analysis is devoted only to Padé signal processing using both nonparametric and parametric estimations. Regarding the derivative analysis, the reason for employing the parametric Padé estimation is to cross-validate the findings from the nonparametric Padé processing. This validation is done on two levels. First, Fig. 5 shows total shape spectra (nonderivative, derivative) in the nonparametric and parametric Padé versions. Second, Fig. 6 displays component spectra (FPT and dFPT, both parametric) as well as the nonparametric FPT and dFPT. All these spectra are in the magnitude mode alone. The derivative order $m$ runs from 1 to 4 as in Figs. 3 and 4. The same Padé order or model order $K = 180$ is used in Figs. 5 and 6 for the nonparametric and parametric Padé estimations.

The importance of complex nonderivative spectra is in the fact that they are the starters for obtaining derivative complex spectra. Such starters can be either complex envelopes (for nonparametric derivatives) or complex components (for parametric derivatives). Once complex spectra (nonderivative, derivative, parametric, nonparametric, components, envelopes) are computed, their magnitude modes are thereafter selected for plotting in Figs. 5 and 6.

Figure 5 compares the results for Padé parametric (panels a–c,g,i) and nonparametric envelopes (panels d–f,h,j) with and without the derivative transforms. Thus, the nonderivative findings by the parametric and nonparametric FPT are on panels (a) and (d), respectively. On the other hand, panels (b,c,e,f,g–j) are all for the dFPT in the parametric (panels b,c,g,i) and nonparametric (panels e,f,h,j) estimations. It is gratifying to see in Fig. 5 that there is full agreement (down to the smallest spectral structure) between all the nonparametric and parametric estimations of Padé envelopes. Most importantly, such a concordance of the two completely different algorithms of Padé processing extends not only to the main resonances on panels (a) and (d) for the nonderivative FPT, but also to the shown four derivatives, $|D_1\text{FPT}|$ (b,e), $|D_2\text{FPT}|$ (c,f), $|D_3\text{FPT}|$ (g,h) and $|D_4\text{FPT}|$ (i,j).

This fully cross-validates the Padé nonparametric derivative total shape spectra for the studied subject. In fact, it is equally correct to state that the nonparametric

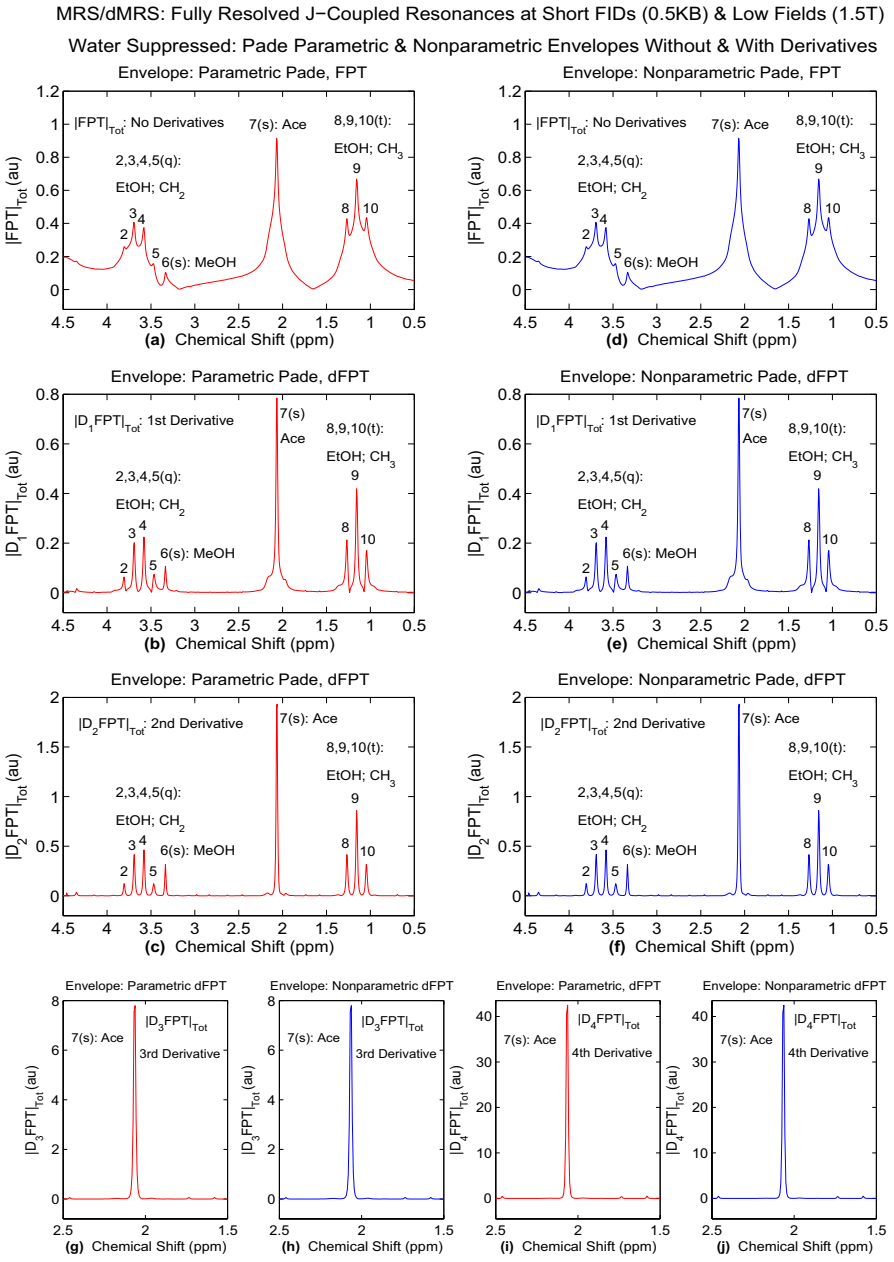


**Fig. 5** MRS and dMRS for the standard Philips Phantom A [22, 23] with the main content: ethanol, methanol, acetate and water. Processing of time signals of short length $N = 512$ encoded with water suppression at a 1.5T GE clinical scanner. No residual water suppression. Nonderivative and derivative Padé envelopes with no zero filling: parametric (**a**, **b**, **c**, **g**, **i**) and nonparametric (**d**, **e**, **f**, **h**, **j**). Abscissae in ppm, ordinates in arbitrary units (au). For details, see the main text (Color figure online)

and parametric estimations cross-validate each other. For both the nonderivative and derivative versions, the coincidences of total shape spectra between the parametric and nonparametric predictions have a deeper significance, which goes beyond verifications of two different Padé computational algorithms.

Namely, a total shape spectrum (2.9) in the parametric FPT (nonderivative) is generated by first reconstructing all the component spectra (2.8) for every resonance and then performing their Heaviside summations. The parametric derivative envelopes follow from applying the derivative operator $\mathrm{D}_m$ to the Heaviside partial fraction sum (2.9). In contradistinction, a total shape spectrum (2.3) in the nonparametric FPT (nonderivative) stems from a pure estimation process of the overall lineshape, with no reference to any component spectrum. When such a source envelope (nonderivative) is subjected to $\mathrm{D}_m$, the derivative envelopes would follow in the nonparametric dFPT and these are not computed from any components either. That is why it is fascinating to have full agreement in Fig. 5 between the nonparametric and parametric Padé spectra on both the nonderivative (panels a, d) and derivative (b vs. e, c vs. f, g vs. i and h vs. j) levels.

Generally, parametric signal processors do not give the exact solution of the quantification problem, which consists of reconstructing all the peak positions, widths, heights and phases of each resonance. This implies nonuniqueness of the solutions meaning that, possibly, widely different sets of component spectra (built from the retrieved peak parameters) can still yield nearly the same envelopes (within the boundaries of the prescribed accuracy)[5]. This limits the practical usefulness of cross-validations merely on the envelope level for the given two methods against each other (or two or more variants of the same methodology).

However, such remarks do not apply to the fast Padé transform in any of its variants. The reason is in the most important feature of Padé signal processing: all its reconstructions are unique. This occurs after full convergence has been attained by systematically increasing the model order, as also discussed in a recent review [30]. In particular, the Padé solution of the standard, nonderivative quantification problem is exact, signifying that there is only one set of the component spectra (hence uniqueness). This gives the solid basis to all the comparisons in Fig. 5 between the Padé envelopes computed nonparametrically and parametrically for both nonderivative and derivative predictions.

It is interesting to note that in e.g. Fig. 5f, the average resonance frequency $\bar{\nu}_\mathrm{R}$ of methyl $CH_3$ protons is smaller than that of methylene $CH_2$ protons in ethanol. This is understood in terms of the meaning of chemical shift. A resonance frequency is determined by an effective magnetic field $B_0^{(\mathrm{eff})} = B_0 - \sigma$, experienced by a proton in $^1$H MRS. Here, the displacement $\sigma > 0$ is due to shielding of the external static magnetic field $B_0$ by electrons in the given group of ethanol. The greater the shielding of $B_0$, the smaller the screened field $B_0^{(\mathrm{eff})}$, the lower the resonance frequency $\bar{\nu}_\mathrm{R}$. Shielding is larger in $CH_3$ than in $CH_2$, i.e. $\sigma(\mathrm{CH_3}) > \sigma(\mathrm{CH_2})$, implying $B_0^{(\mathrm{eff})}(\mathrm{CH_3}) < B_0^{(\mathrm{eff})}(\mathrm{CH_2})$, so that $\bar{\nu}_\mathrm{R}(\mathrm{CH_3}) < \bar{\nu}_\mathrm{R}(\mathrm{CH_2})$ and this is what is seen in Fig. 5f.

[5] The nonuniqueness of the solutions translates into the nonexistence of the solutions.

It should be born in mind that, in general, shielding of $B_0$ at the location of a spin-active nucleus is not obtained by simply counting the number of electrons in a given molecule. The procedure is much more involved because of several intervening factors (charge distribution of electronic clouds associated with various orbitals that determine the given state of a molecule, nonspherical interaction potentials, multicenter character of molecules preventing a simple diamagnetic circulation of electrons about a single nucleus, etc) [38].

It is pertinent here to refer to Arnold's memorable return to the ethanol problem in 1956 [37] with much more accurate measurements than in the earlier epic experiments from 1951 by Arnold, Dharmatti and Packard [21]. He constructed a larger permanent magnet with a significant reduction of field inhomogeneities and recorded a fine splitting in ethanol. This time, the acquired spectrum[6] of ethanol contained novel features via eight resonances, a triplet (1:2:1) for $CH_3$, a quartet (1:3:3:1) for $CH_2$ and a singlet for OH, where the proportions in the parentheses are the peak area ratios estimated from the experimental data [37]. These latter ratios were in agreement with the calculations by Arnold [37] who used the quantum-mechanical perturbation theory.

Regarding the most intriguing resonances, the $CH_3$ triplet and the $CH_2$ quartet, the measured spectrum of ethanol (the top panel of Fig. 6b in Ref. [37]) is extremely similar, even to the finest details, to the present Fig. 5f for the dFPT in the second derivative $|D_2FPT|_{Tot}$. This agreement is highly significant as it indicates that in the mixture of molecules from the presently studied Proton Phantom [22, 23], the presence of methanol (#6) and acetate (#7) does not alter the intrinsic spectrum of ethanol (##2–5,8–10). This may imply that the spin-spin interactions of ethanol protons with protons from methanol and acetate are sufficiently weak (with a negligible small coupling constant) to obscure any further J-splitting.

Comparison on the level of the Padé envelopes alone from Fig. 5 is necessary, but not sufficient to complete the analysis. It still lacks a key finding, which is information about the component spectra. These are inherently present, yet invisible in the parametrically generated Padé envelopes. In order to fulfill also the sufficient condition for full validation of Padé derivative nonparametric estimations, we provide Fig. 6. This figure explicitly discloses the component spectra (nonderivative, derivative) from the Padé parametric estimations. These components are placed side by side with the associated nonparametrically computed total shape spectra.

In Fig. 6, panels (a-c,g,i) are for the component spectra from the parametric Padé reconstructions, whereas panels (d-f,h,j) are allocated to the nonparametric Padé envelopes. Prior to plotting Fig. 6, we verified in the parametric Padé (nonderivative, derivative) that all the component spectra give the corresponding parametric Padé envelopes from panels (a-c,g,i) in Fig. 5. This is true only provided that *all* the

[6] In the early years of NMR, spectra were indeed measured. However, for a long time now, this is not the case since FIDs are measured in the time domain and from such experimental data spectra are reconstructed by computations in the frequency domain. Surprisingly, however, still the term "acquired spectra" is abundantly in use in the MRS literature, at variance with what is actually encoded.

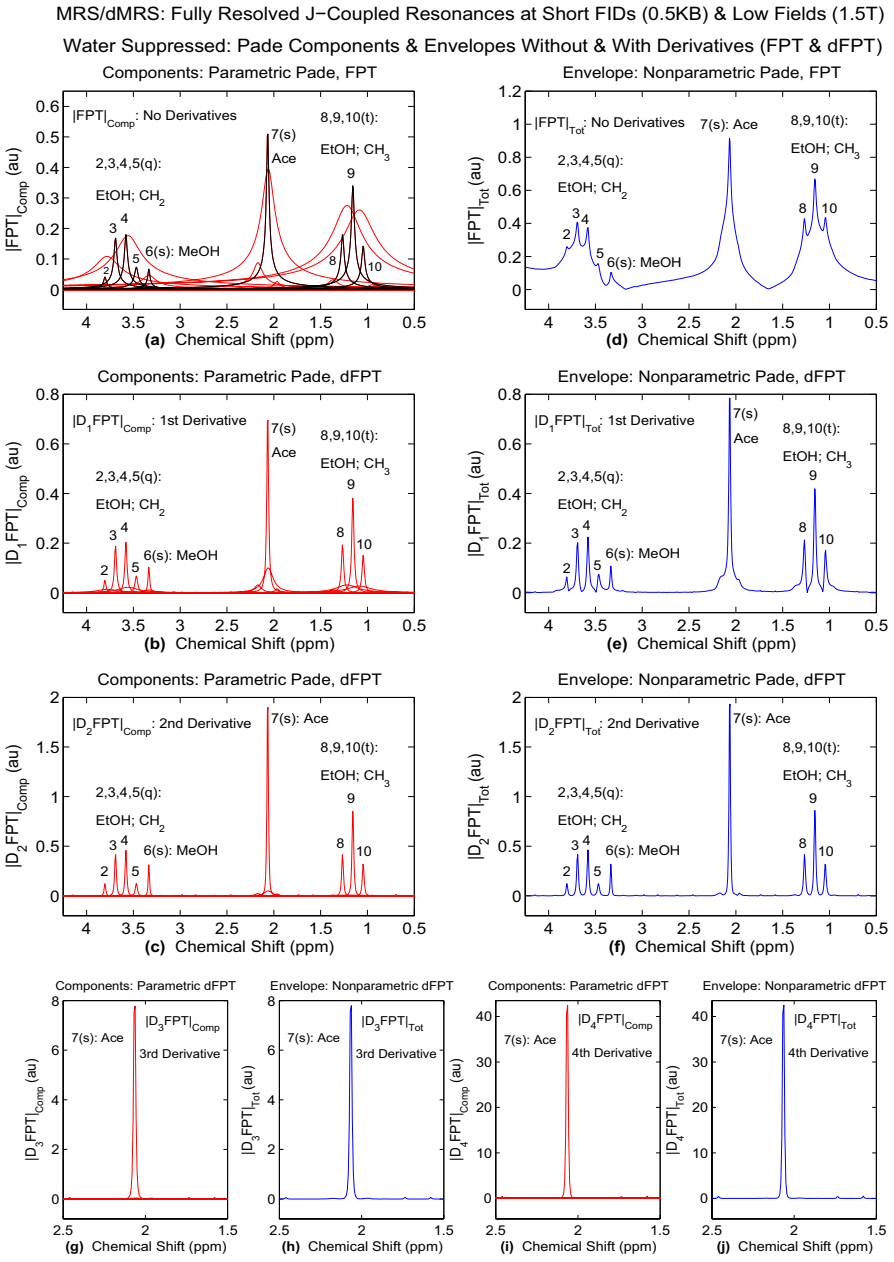


**Fig. 6** MRS and dMRS for the standard Philips Phantom A [22, 23] with the main content: ethanol, methanol, acetate and water. Processing of time signals of short length $N = 512$ encoded with water suppression at a 1.5T GE clinical scanner. No residual water suppression. Nonderivative and derivative fast Padé transform with no zero filling: parametric components (**a**, **b**, **c**, **g**, **i**) and nonparametric envelopes (**d**, **e**, **f**, **h**, **j**). Abscissae in ppm, ordinates in arbitrary units (au). For details, see the main text (Color figure online)

components are summed up to deduce the considered total shape spectrum. However, to avoid clutter on panel (a) of Fig. 6 and, most importantly, to focus primarily on ethanol, methanol and acetate, we have not plotted the unessential elevated tails of the derivative components from the residual water resonance. As a result, only for the small part near 4.25 ppm, the sum of all the components shown in panel (a) is slightly lower than the corresponding nonparametrically generated envelope (panel d). However, elsewhere on the chemical shift axis, the sum of all the displayed components from panel (a) equals the associated parametric envelope from panel (d). This occurs because the tails of the derivative components from the residual water resonance are of short range (i.e. they do not extend far from the central water peak at 4.87 ppm).

Panel (a) in Fig. 6 is pivotal. It shows the component spectra from applying the nonderivative parametric Padé to the encoded time signal. These components are the gold standard because they stem from the reconstructed exact and, hence, unique peak parameters (positions, widths, heights, phases) of every physical resonance, the concluding goal of quantification.

For a clearer visual distinction, all the components (parametric Padé) in Fig. 6 are drawn as red curves, whereas the blue curves are for the envelopes (nonparametric Padé). Exceptionally, on panel (a), for highlighting, the same red spectra for the (main) nine resonance components $\#\#2-10$ (ethanol, methanol, acetate) are redrawn as brown curves. Besides the principal, sharp resonances ($\#\#2-10$) within the frequency band $\nu \in [0.5, 4.25]$ ppm, panel (a) of Fig. 6 also contains a number of other resonances (some of them are quite broad).

On panel (a) in Fig. 6, the largest broad peaks are concentrated near ethanol, methanol and acetate. This pattern is similar to those from *in vivo* $^1$H MRS spectra of e.g. human brain, where resonances of a few among many diagnostically relevant metabolites (e.g. Lac, NAA, Glu, Cr and Cho)[7] are heavily surrounded by wide peaks usually assigned to various macromolecules (proteins, lipids,...). Although the broad resonances are prominently present on panel (a) in Fig. 6, they are nevertheless left unassigned. This is because in building the envelope, these wide resonances play the role of a background alongside the tails of the components of the water peak.

The spin-spin relaxation time ($T_2^\star$) of a resonance is inversely proportional to the spectral breadth (width). This means that a broader/narrower peak corresponds to a shorter/longer $T_2^\star$, associated with a faster/slower decaying resonance, respectively.

Because of these diametrically opposite patterns, broad and narrow resonances undergo different changes for the same derivative order $m$. This occurs despite the fact that in the dFPT, *all* resonances (wide and sharp alike) in a spectrum become progressively thinner and simultaneously taller with increasing $m$. However, the rates of the peak growth are smaller/larger for broader/narrower resonances, respectively. This leads to an increased dynamic range of the peak heights (ordinate)

[7] Lac: 1.33 ppm (a doublet separated by $J = 7$Hz: the methyl $CH_3$ group of Lac), NAA: [2.02 ppm (the methyl $CH_3$ group of NAA), 2.47-2.66 ppm (the methylene $CH_2$ group of NAA)], Glu: [2.04, 2.11 ppm (the methylene $CH_2$ group of Glu), 2.35 ppm (the methyl $CH_3$ group of Glu)], Cr: [3.04 ppm (the methylene $CH_2$ group of Cr), 3.93 ppm (the methyl $CH_3$ group of Cr)], Cho: [3.22 ppm (the methyl $CH_3$ group of Cho), 4.05 ppm (the methylene $CH_2$ group of Cho)].

versus chemical shifts (abscissa) when attempting to plot (on the same graph) all the resonances with different widths. In such figures, broader resonances will be on their way of disappearing for increasing $m$, leaving behind as visible the sharper peaks alone.

This is precisely what is seen in Fig. 6 on panels (b) and (c) for the component spectra due to the Padé parametric first and second derivatives, $|D_1FPT|_{Comp}$ and $|D_2FPT|_{Comp}$, respectively. Already $|D_1FPT|_{Comp}$ (panel b) is able to massively diminish all the broad tall peaks. Regarding the wide resonances, the leftovers from their first huge suppression on panel (b), are practically annulled by $|D_2FPT|_{Comp}$ (panel c) everywhere in the band [0.5, 4.25] ppm, excepting the three minuscule bumps on the bottom of the acetate peak. However, these minor remainders are completely washed out by the third and fourth component derivatives $|D_3FPT|_{Comp}$ and $|D_4FPT|_{Comp}$ on panels (g) and (i), respectively.

To summarize the left top column in Fig. 6, it is seen that the component non-derivative spectra $|FPT|_{Comp}$ (panel a), initially congested with broad resonances, became much sparser in $|D_1FPT|_{Comp}$ (panel b) and basically void of broad peaks in $|D_2FPT|_{Comp}$ (panel c). This implies that the so-named "spectral crowding" [39–41] can largely be mitigated by derivative estimations in the dFPT. It also means that the parametric dFPT achieves visual separations of sharp and broad resonances in a sequential manner. First fully visualized are sharp resonances because their smaller widths determine the size of the ordinates in the graphs of spectral intensities as a function of chemical shifts. Subsequently visualized are broad resonances. This is achieved by e.g. significantly reducing the maximal values at the ordinates to allow wider resonances to pop out on the adjusted plot.

The fact that broad resonances are perceivably absent from the second derivative $|D_2FPT|_{Comp}$ (panel c) does not mean that they disappeared altogether. Just the opposite is true as, in fact, they persist, but are hidden underneath the sharp and much taller resonances. In addition to the mentioned ordinate size reduction, the broader resonance components can become visible in an alternative manner by subtracting the sharper resonance components from all the resonance components (sharp+broad) from panel (c), i.e. $|D_2FPT|_{Broad\ Comp} = |D_2FPT|_{All\ Comp} - |D_2FPT|_{Sharp\ Comp}$. By design, the lineshapes $|D_2FPT|_{Broad\ Comp}$ can alternatively be referred to as 'the annulled sharp resonance spectra'. In MRS, these difference spectra could be referred to as 'spectra void of the recognized diagnostically relevant metabolites'.

In comparing the parametric with nonparametric dFPT in Fig. 6, using the first derivatives $|D_1FPT|_{Comp}$ (panel b) and $|D_1FPT|_{Tot}$ (panel e), a large extent of concordance is obvious. Nevertheless, it can be seen that the resonance intensities of peaks ##2–10 in the first derivative $|D_1FPT|_{Comp}$ (panel b) and $|D_1FPT|_{Tot}$ (panel e) do not coincide. They are higher for $|D_1FPT|_{Tot}$ than for $|D_1FPT|_{Comp}$. The reason is in the presence of the smaller leftovers of broad resonances around peaks ##2–10 in $|D_1FPT|_{Comp}$ (panel b).

These spectral leftovers are added to the lineshapes of the component peaks ##2–10 to generate the parametric envelope $|D_1FPT|_{Tot}$. The latter parametric envelope, in turn, matches the nonparametric envelope $|D_1FPT|_{Tot}$ as per Fig. 5 (panels b,e). This latter nonparametric envelope $|D_1FPT|_{Tot}$ is also present in Fig. 6e. Thus, the peak heights of resonances ##2–10 in the nonparametric envelope $|D_1FPT|_{Tot}$

(Fig. 6e) are higher than their counterparts in $|D_1FPT|_{Comp}$ (Fig. 6b) because the former (being the total shape spectrum), implicitly includes the remainders of the hidden broader resonances.

Next in line to analyze in Fig. 6 are the component spectra $|D_2FPT|_{Comp}$ (panel c) from the parametric dFPT and the envelope $|D_2FPT|_{Tot}$ (panel f) due to the nonparametric dFPT. Here, remarkably, around methanol (#6) and both groups ($CH_2$ , $CH_3$) of ethanol, all the component spectra $|D_2FPT|_{Comp}$ from parametric Padé processing in panel (c) are seen to collapse into the single nonparametric envelope $|D_2FPT|_{Tot}$ from panel (f). In particular, the peak heights in the triplet $CH_3$ group of ethanol (##8–10), the singlet of methanol (# 6) and the quartet $CH_2$ group of ethanol (##2–5) in the components (panel c, parametric dFPT) coincide with their counterparts in the envelope (panel f, nonparametric dFPT).

Only the peak height of acetate on panel (f) is slightly higher in the envelope $|D_2FPT|_{Tot}$ than in the acetate component from $|D_2FPT|_{Comp}$ on panel (c). This is caused by the contribution from a small peak lying within the lineshape of acetate. Finally, this minimal difference vanishes by resorting to the third derivative of the parametric (components) and nonparametric (envelopes) in the dFPT. This is shown by $|D_3FPT|_{Comp}$ (panel g) and $|D_3FPT|_{Tot}$ (panel h). The identical peak heights of acetate are also obtained in the fourth derivatives $|D_4FPT|_{Comp}$ (parametric dFPT, panel i) and $|D_4FPT|_{Tot}$ (nonparametric dFPT, panel j). This double check on panels (i) and (j) for the fourth derivatives was optional since the third derivatives on panels (g) and (h) completed the verification for the peak height of acetate.

Quantification in NMR spectroscopy is aimed at finding the peak parameters from nonderivative rather than from derivative spectra. Nevertheless, this poses no problem due to the existence of the conversions (by simple scaling factors) from the found derivative peak parameters to the sought nonderivative peak parameters [29]. Thus, we can extract the peak parameters from the nonparametric dFPT (e.g. $|D_2FPT|_{Tot}$, Fig. 6f) and scale them to arrive at the peak parameters associated with $|FPT|_{Comp}$ (Fig. 6a) in the nonderivative parametric FPT, as will be reported shortly. If instead of the magnitude mode, absorption is desired, another straightforward scaling of the peak width by a factor of $\sqrt{3}$ would suffice.

Overall, with respect to the peaks ##2–6 and ##8–10 in Fig. 6, the extent of agreement between the parametrically produced components $|D_2FPT|_{Comp}$ (panel c) and the nonparametric total shape spectrum $|D_2FPT|_{Tot}$ (panel f) is indeed impressive. The same holds true for the peak #7 (acetate) from $|D_3FPT|_{Comp}$ (panel g, components) and $|D_3FPT|_{Tot}$ (panel h, envelope) as well as from $|D_4FPT|_{Comp}$ (panel i, components) and $|D_4FPT|_{Tot}$ (panel j, envelope). No resonances ##2–6 or ##8–10 are shown in $|D_{3,4}FPT|_{Comp}$ nor $|D_{3,4}FPT|_{Comp}$. The reason is in the fact that $|D_2FPT|_{Comp}$ (panel c) and $|D_2FPT|_{Tot}$ (panel f) furnish the final lineshapes (with no bumps underneath) for these resonances (methanol and the two groups of ethanol).

The moral of this story is far reaching given that we started with the nonparametric dFPT which, in principle, can reconstruct only derivative total shape spectra. In other words, computations by the nonparametric dFPT never deal explicitly with any component spectrum underlying the reconstructed envelope. Yet, this nonparametric envelope (panel f) is found to smoothly merge into its own components from which it finally becomes indistinguishable and identical to the parametric components from

panel (c). In other words, the envelope in panel (f), born out from the nonparametric dFPT, turns out to be identical to the components due to the parametric dFPT. This is where the parametric dFPT steps in as the ultimate judge of the veracity of the nonparametric dFPT.

In hindsight, by reference to our earlier studies [27–29], one would expect that high-order derivative estimations in the dFPT would meet with success in observing full agreement between nonparametric envelopes and parametric components. The big surprise, however, of the present study is that such agreement has been recorded already with the second-order derivatives, as per panels (c) and (f) in Fig. 6.

### 3.4 Separation of macromolecules from the main metabolites

For *in vivo* MRS, the discussed derivative sequential reconstructions (first sharp and then broad peaks) can be used as an optimal and objective way to extract and analyze macromolecules separately from the main metabolites. Human tissue and living cells abundantly contain water to within 60-70%. To mimic this situation, spectroscopic phantoms (GE brain phantom, Philips Phantom A, etc) include chemical compounds dissolved in water whose volume largely surpasses the volumes of other substances. As a result, in applications of $^1$H MRS to biomedical samples, the water resonance line dominates (by a factor of $\sim$ 500-1000 for spectroscopic phantoms) over all the other spectral lines, as is also clear from the present Figs. 1 and 2. This is even more true for *in vivo* $^1$H MRS where the water peak overwhelms (by a factor of $\sim$ 10000) all resonance proton lines stemming from proteins, lipids, nucleotides, hydrocarbons and other chemical compounds.

In most cases, resonance lines from various metabolites exhibit rather involved structures that, in turn, suggest the presence of partially overlapping resonance lines. Moreover, resonances assigned to some of the recognized diagnostically informative metabolites (Lac, NAA, Glu, m-Ins, Cre, Cho, ...) overlap with those from macromolecules. For example, the lactate doublet is barely visible around 1.33 pm in spectra from normal, healthy tissue because of a heavy overlap with considerably broader lipid resonances (reminiscent of what is seen in Fig. 6a around ethanol, methanol and acetate).

In practice, to separate the overlapping lactate and lipids, FIDs are encoded usually with two echo times, TE, e.g. 24 and 136 ms. The latter TE would give the Lac doublet inverted (negative peaks, pointed downward), while the resonances from lipids will not change their phases. This requires extra measurements, which can be avoided altogether by exploiting the sequential resolutions (very convenient for visual monitoring) achievable with the dFPT. This derivative signal processor, just like in Fig. 6, would pull out the sharp lactate doublet because the broader lipid resonances would temporarily disappear. The lipid resonances can subsequently reappear for visualization (and, most importantly, for quantification) by reducing the scale of the ordinate to match their peak heights (or by the described procedure of 'annulling the main resonances').

This particular subject is of great importance for tumor diagnostics of various human organs by *in vivo* $^1$H MRS and we shall deal with it in a separate report

using the dFPT. Ordinarily, macromolecules are not viewed to be of primary diagnostic relevance. For this reason, their presence in spectra is usually viewed as a burden, which blocks visual resolution of the diagnostically important metabolites. For *in vivo* $^{1}$H MRS, the main metabolite resonances (Lac, NAA, Glu, Cre, Cho, ...) are superimposed on some rolling backgrounds, that are partially created by macromolecules.

The customary practice is to treat such a rolling baseline as a nuisance and fit it by a 3- or 4-degree spline polynomial. The outcome is subsequently subtracted from the complete spectrum for a presumably easier fitting. One of the obvious disadvantages of this recipe is that the fitting polynomial can capture (and, thus, throw out by the said subtraction) some of the weak resonances of diagnostic relevance, e.g. phosphocholine (PCho).

By contrast, when appropriately processed by the dFPT, macromolecular resonances (as well as whatever else hides in rolling baselines), are reliably separated from the main metabolites without losing any information. Moreover, every resonance from this background baseline, including those due to macromolecules, after a proper identification by the dFPT, can be quantified similarly to the main metabolites. In other words, the dFPT would give a proper status to macromolecules treating them on the same footing as metabolites of presumed top diagnostic priority. Moreover, this could considerably enlarge the existing metabolite database [42] by adding the dFPT-estimated macromolecular spectral characteristics[8]. Thus, we see that the sequential convergence of resonances translates into a reliable procedure for differentiating between the two groups of spectral structures, the main metabolites and macromolecules. This could be clinically useful.

The expounded correct approach to macromolecules using the dFPT would leave no room to their often stated misinterpretations yielding potentially ambiguous diagnostic evaluations in the clinic. For example, differentiating acute and chronic multiple sclerosis by MRS may well depend on the way in which macromolecules (proteins, peptides, lipids) are interpreted when they reside near the main metabolites. In the past, there were several medical studies [44–51] that interpreted the detected elevated levels of metabolites in the spectral range of lipids as indications of acute lesions.

However, lipids could well be among the significant (if not leading) contributors to the metabolites' elevated levels. Had macromolecules been properly taken into account, to assess their impact on the enhanced intensities of main metabolite resonances, the diagnosis could have been different (possibly chronic multiple sclerosis). In Refs. [44–51], contamination of metabolite resonances by lipids has not been estimated by measurements either. For example, these studies performed no outer volume saturation to rule out lipid contamination possibly due to the fat-containing structures in the skull.

When properly isolated and quantified by the dFPT, macromolecules could actually be diagnostically invaluable in several spectral regions around e.g. 0.93, 1.24,

[8] Spectral parameters of several macromolecules have been estimated in e.g. Ref. [43] by fitting.

1.30, 1.43, 2.05, 3.05 ppm. For instance, in the discussed multiple sclerosis example, by reference to the data from persons in a control group, one could differentiate between acute and chronic lesions using the estimated levels of macromolecules if they are significantly higher in one than in the other group of patients. Such a differential diagnosis in multiple sclerosis has been addressed e.g. in Refs. [52–54]. A study along the lines of Ref. [54], dealing with detection of macromolecules in $^1$H MRS spectra from the human brain, has been reported in Ref. [55].

## 4 Conclusion

This study is on the problem of J-coupled resonances in magnetic resonance spectroscopy, MRS. Signal processing methods are used to resolve the encountered multiplets under restrictive conditions. These involve short time signals (512 data points), encoded with water suppression (by inversion recovery) at a clinical scanner of a low magnetic field strength (1.5T). The encoded time signals and the reconstructed spectra are presented and thoroughly analyzed.

Data analysis is carried out by using the standard, nonderivative fast Padé transform, FPT, as well as its derivative version, dFPT. Both the shape and parameter estimations are performed with the FPT and dFPT. To place the reported Padé-based reconstructions into perspective, as well as to allow the necessary comparisons, the nonderivative and derivative fast Fourier transforms, FFT and dFFT, respectively, are also employed in the present computations and analysis. However, the main emphasis in this work is placed onto the dFPT.

The object of encoding (in the time domain) and spectral reconstructions (in the frequency domain) is a spectroscopic phantom. We chose the Philips Phantom A for proton MRS. It is a polyethylene plastic sphere filled with a number of known chemical compounds dissolved in demineralized water. The most important molecules in this phantom are ethanol (ethyl alcohol), methanol (methyl alcohol) and acetate (acetic acid). The sought spectral structure is comprised of the main nine resonances: the two singlets (methanol, acetate) and the seven J-coupled resonances from ethanol. The latter multiplets are the methyl $CH_3$ triplet and the methylene $CH_2$ quartet, with the intensity ratios of the individual lines 1:2:1 and 1:3:3:1, respectively, as per the Pascal triangle. The hydroxyl OH group of ethanol is swamped by the dominant water peak and, as such, was not in our focus.

The overall goal is to fully resolve these nine peaks, including the multiplets, the seven J-coupled resonances (all the way to nearly zero-valued background baseline) by means of the dFPT as a shape estimator applied to the encoded raw time signals (no zero filling) from which water has been suppressed during measurements. Moreover, the water residual has not been suppressed by signal processing.

Regarding the standard, nonderivative shape estimations, no method could resolve all the nine resonances. This is caused by an elevated background baseline which generated tight overlaps among most resonances. Such a situation gives a chance to try some other kinds of envelope estimations. With this goal, derivative nonparametric estimators have been tried here by employing the dFPT and dFFT.

One of the outcomes is that the dFFT is highly unsatisfactory due to the lack any of systematics. Initially, within the dFFT, the first derivative is better than the corresponding nonderivative Fourier, i.e. the FFT. However, the second derivative is deteriorated relative to its first counterpart in the dFFT. Yet worse, with higher derivatives, most of the nine resonances are smashed into the background baseline and, as such, wiped out from the spectrum.

Such failures are ascribed to the way in which the $m$th order derivative operator $(\mathrm{d}/\mathrm{d}\nu)^m$, with respect to the sweep linear frequency $\nu$, acts on the source of the FFT, the Fourier integral over the time variable, $t$. In the integrand of the Fourier integral, the general derivative operator $(\mathrm{d}/\mathrm{d}\nu)^m$ produces a time power function ($\sim t^m$), which therein multiplies the encoded time signal, $c(t)$. The digitized version of the ensuing product function $\sim t^m c(t)$ is Fourier-processed to yield the envelopes in the dFFT.

This procedure in the FFT decreases SNR because the power $m$ of the multiplying term $t^m$ is augmented with the increased derivative order $m$. The modulated function $t^m c(t)$ weighs heavily larger values of $t$ dominated by the noisy part of the encoded time signal, $c(t)$. Eventually, noise prevails in the envelopes from the dFFT. This, in turn, annuls all the physical resonances and, in the end, the dFFT is left with noise alone.

In sharp contrast, shape estimations by the nonparametric dFPT fully met the challenge by completely resolving all the sought nine resonances. Especially enlightening was to record (already in the second derivative from the dFPT) a perfect splitting apart of the J-coupled resonances of ethanol with the correct peak area ratios. The success of the dFPT is in processing directly the encoded time signals $c(t)$, free from any weight function, to yield a flattened background baseline as well as narrower and taller resonances with increased derivative order $m$. This automatically translates into simultaneously improved resolution and SNR.

Moreover, for total shape spectra, the derivative Padé, dFPT, hugely outperforms its nonderivative counterpart, FPT. This is a very important boost to the dFPT, not only for problems involving spectroscopic phantoms with the known contents (that represent an optimal testing ground for any estimator), but also to other problem areas. Examples are time signals encoded either from samples whose constituents are yet to be determined or from patients in applications of MRS to diagnostics in radiology.

Expectedly, component shape spectra from the nonderivative parametric FPT reached the stated goal in full. Herein, the ensuing unique reconstructions can serve as the gold standard for cross-validations of any other estimations. In the validations of the dFPT, the most fascinating is our finding that there is a full coincidence of the second derivatives of the nonparametrically computed envelope with the corresponding components from the exact solutions of the quantification problem in parametric estimations.

This coincidence implies that the nonparametric dFPT, as a shape estimator, actually solves the quantification problem exactly. The resonances found by the nonparametric dFPT offer an easy way to the sought peak parameters. For instance, as an initial insight, one can rely on visual resolutions of isolated Lorentzian resonances from envelopes due to shape estimations by the dFPT. This is achieved by reading

off directly the peak positions, widths and heights on the screen which shows the derivative envelopes in the magnitude mode. The peak height and the peak width automatically yield the peak area, which is the key to determining the number of the equivalent protons that contributed to the given resonance. Independently and more accurately, the same computer program for these Lorentzian lineshapes can also provide the output linelist of derivative peak parameters. Finally, the concluding step is to pass from the derivative to the nonderivative absorptive peak parameters. For this all that is needed is to use the conversion factors available from Ref. [29].

Information on peak areas of resonances is the prerequisite for extraction of metabolite concentrations, the ultimate goal of signal processing as it applies to medicine, particularly to tumor diagnostics using MRS [32–34]. This is precisely where we are heading in the future with the Padé derivative methodology for which the present benchmarking is of utmost importance. It directly addresses most of the troubles that hamper the entry of proton MRS into the standard diagnostic armamentarium in the clinic, e.g. relatively low SNR, insufficient resolution, overlapping resonances, macromolecular interference, abundant unresolved multiplets due to nuclear spin-spin interactions (J-coupling), etc. These long-lasting obstacles to clinical nuclear magnetic resonance spectroscopy can all simultaneously be circumvented by the derivative magnetic resonance spectroscopy, dMRS, when signal processing is carried out with the dFPT.

**Acknowledgements** The authors thank two Research Funds: Radiumhemmet via the Karolinska University Hospital and the Stockholm County Council (FoUU). Open Access has been provided by the Karolinska Institute, Stockholm, Sweden.

**Funding** Open Access funding provided by Karolinska Institute.



## References

1. I. Estermann, O. Stern, Beugung von molekularstrahlen. Z. Phys. **61**, 95–125 (1930)
2. I.I. Rabi, Space quantization in a gyrating magnetic field. Phys. Rev. **51**, 652–654 (1937)
3. I.I. Rabi, J.R. Zacharias, S. Millman, P. Kusch, A new method of measuring nuclear magnetic moment. Phys. Rev. **53**, 318 (1938)
4. I.I. Rabi, S. Millman, P. Kusch, J.R. Zacharias, The molecular beam resonance method for measuring nuclear magnetic moments. The magnetic moments of $^{3}Li^{6}$, $^{3}Li^{7}$ and $^{9}F^{19}$. Phys. Rev. **55**, 526 (1939)
5. C.J. Groter, Negative results of an attempt to detect nuclear magnetic spins. Physica **9**, 995–998 (1936)
6. F. Bloch, W.W. Hansen, M. Packard, Nuclear induction. Phys. Rev. **69**, 127 (1946)

7. F. Bloch, Nuclear induction. Phys. Rev. **70**, 460–474 (1946)
8. F. Bloch, W.W. Hansen, M. Packard, The nuclear induction experiment. Phys. Rev. **70**, 474–485 (1946)
9. E.M. Purcell, H.C. Torrey, R.V. Pound, Resonance absorption by nuclear moments in a solid. Phys. Rev. **69**, 37–38 (1946)
10. E.M. Purcell, N. Bloembergen, R.V. Pound, Resonance absorbtion by nuclear magnetic moments in a single crystal of $CaF_2$. Phys. Rev. **69**, 988 (1946)
11. K. Siegbahn, G. Lindström, Magnetic moments of deuterium-2, lithium-7 and fluorine-19. Nature **163**, 211 (1949)
12. K. Siegbahn, G. Lindström, The nuclear magnetic moments of $D^2$, $Li^7$ and $F^{19}$ studied by the magnetic resonance absorption method. Arkiv f. Fysik **1**, 193–213 (1949)
13. W.G. Proctor, F.C. Yu, On the Magnetic Moments of $Mn^{55}$, $Co^{59}$, $Cl^{37}$, $N^{15}$ and $N^{14}$. Phys. Rev. **77**, 716–717 (1950)
14. W.G. Proctor, F.C. Yu, The dependence of a nuclear magnetic resonance frequency upon chemical compound. Phys. Rev. **77**, 717 (1950)
15. W.C. Dickinson, Dependence of the $F^{19}$ nuclear resonance position on chemical compound. Phys. Rev. **77**, 736–737 (1950)
16. G. Lindström, An experimental investigation of the nuclear magnetic moments of $D^2$ and $H^1$. Phys. Rev. **78**, 817–818 (1950)
17. H.A. Thomas, The diamagnetic correction for protons in water and mineral oil. Phys. Rev. **77**, 901–902 (1950)
18. G. Lindström, Nuclear resonance absorption applied to precise measurements of nuclear magnetic moments and the establishment of an absolute energy scale in $\beta$−spectroscopy. Arkiv f. Fysik **4**, 1–80 (1951)
19. H.C. Gutowsky, R.E. McClure, Magnetic shielding of the proton resonance in $H_2$, $H_20$ and mineral oil. Phys. Rev. **81**, 276–277 (1951)
20. W.C. Dickinson, The time average magnetic field at the nucleus in nuclear magnetic resonance experiments. Phys. Rev. **81**, 717–731 (1951)
21. J.T. Arnold, S.S. Dharmatti, M.E. Packard, Chemical effects on nuclear induction signals from organic compounds. J. Chem. Phys. **19**, 507 (1951)
22. Manual, Spectroscopy Application Guide Gyroscan ACS-NT. Philips Medical System Nederland B.V. (1989)
23. Manual, Philips Medical System Nederland B.V. (2014). Release 5-US-Version (www.philips.com/healthcare)
24. D.J. Drost, W.R. Riddle, G.D. Clarke, Proton magnetic resonance spectroscopy in the brain: Report of AAPM MR Task Group #9. Med. Phys. **29**, 2177–2197 (2002)
25. Dž. Belkić, K. Belkić, Quantification by the fast Padé transform of magnetic resonance spectroscopic data encoded at 1.5T: implications for brain tumor diagnostics. J. Math. Chem. **54**, 602–655 (2016)
26. Dž. Belkić, K. Belkić, Derivative NMR spectroscopy for J-coupled multiplet resonances with short time signals (0.5 KB) encoded at low magnetic field strengths (1.5T): Part II, Water Unsuppressed. J. Math. Chem. (2020). https://doi.org/10.1007/s10910-020-0199-y
27. Dž. Belkić, K. Belkić, Exact quantification by the nonparametric fast Padé transform using only shape estimation of high-order derivatives of envelopes. J. Math. Chem. **56**, 268–314 (2018)
28. Dž. Belkić, K. Belkić, Explicit extraction of absorption peak positions, widths and heights using higher order derivatives of total shape spectra by nonparametric processing of time signals as complex damped multi-exponentials. J. Math. Chem. **56**, 932–977 (2018)
29. Dž. Belkić, K. Belkić, Validation of reconstructed component spectra from non-parametric derivative envelopes: comparison with component lineshapes from parametric derivative estimations with the solved quantification problem. J. Math. Chem. **56**, 2537–2578 (2018)
30. Dž. Belkić, K. Belkić, Review of recent applications of the conventional and derivative fast Padé transform for magnetic resonance spectroscopy. J. Math. Chem. **57**, 385–464 (2019)
31. Dž. Belkić, K. Belkić, Feasibility study for applying the lower-order derivative fast Padé transform to measured time signals. J. Math. Chem. **58**, 146–177 (2020)
32. Dž. Belkić, *Quantum-Mechanical Signal Processing and Spectral Analysis* (Taylor & Francis via CRC Press, London, 2005)
33. Dž. Belkić, K. Belkić, *Signal Processing in Magnetic Resonance Spectroscopy with Biomedical Applications* (Taylor & Francis via CRC Press, London, 2010)

34. Dž. Belkić, K. Belkić, Robust high-resolution quantification of time signals encoded by in vivo magnetic resonance spectroscopy. Nucl. Instr. Phys. Res. A **878**, 99–128 (2018)
35. Dž. Belkić, Exact signal-noise separation by Froissart doublets in fast Padé transform for magnetic resonance spectroscopy. Adv. Quantum Chem. **56**, 95–179 (2009)
36. Dž. Belkić, K. Belkić, The general concept of signal-noise separation (SNS): mathematical aspects and implementation in magnetic resonance spectroscopy. J. Math. Chem. **45**, 563–597 (2009)
37. J.T. Arnold, Magnetic resonance of protons in ethyl alcohol. Phys. Rev. **102**, 136–150 (1956)
38. N.F. Ramsey, Magnetic shielding of nuclei in molecules. Phys. Rev. **78**, 699–703 (1950)
39. Dž. Belkić, K. Belkić, In vivo magnetic resonance spectroscopy for ovarian cancer diagnostics: quantification by the fast Padé transform. J. Math. Chem. **55**, 349–405 (2017)
40. B. Liang, L.K. Tamm, NMR as a tool to investigate membrane protein structure, dynamics and function. Nat. Struct. Mol. Biol. **23**, 468–474 (2016)
41. S. Perez Santero, F. Favretto, S. Zanzoni, R. Chignola, M. Assfalg, M. D'Onofrio, Effects of macromolecular crowding on a small lipid binding protein probed at the single-amino acid level. Arch. Biochem. Biophys. **606**, 99–110 (2016)
42. V. Govindaraju, K. Young, A.A. Maudsley, Proton NMR chemical shifts and coupling constants for brain metabolites. NMR Biomed. **13**, 129–153 (2000)
43. U. Seeger, U. Klose, I. Mader, W. Grodd, T. Nagele, Parametrized evaluation of macromolecules and lipids in proton MR spectroscopy of brain diseases. Magn. Res. Med. **49**, 19–28 (2003)
44. J.S. Wolinsky, P.A. Narayana, M.J. Fernstermacher, Proton magnetic resonance spectroscopy in multiple sclerosis. Neurology **40**, 1764–1769 (1990)
45. P.A. Narayana, J.S. Wolinsky, E.F. Jackson, M. McCarthy, Proton MR spectroscopy of gadolinium-enhanced multiple sclerosis plaques. J. Magn. Reson. Imag. **2**, 263–270 (1992)
46. P.A. Narayana, T.J. Dyle, J.S. Wolinsky, Serial proton magnetic resonance spectroscopic imaging, contrast-enhanced magnetic resonance imaging and quantitative lesion volumetry in multiple sclerosis. Ann. Neurol. **43**, 56–71 (1998)
47. H.B. Larsson, P. Christiansen, M. Jensen, J. Fredriksen, A. Heltberg, J. Olesen, O. Henriksen, Localized in vivo proton spectroscopy in the brain of patients with multiple sclerosis. Magn. Reson. Med. **22**, 23–31 (1991)
48. C.A. Davie, C.P. Hawkins, G.J. Barker, A. Brennan, P.S. Tofts, D.H. Miller, W.I. McDonald, Detection of myelin breakdown products by proton magnetic resonance spectroscopy. Lancet (Letter to the Editor) **341**, 630–631 (1993)
49. C.A. Davie, C.P. Hawkins, G.J. Barker, A. Brennan, P.S. Tofts, D.H. Miller, W.I. McDonald, Serial proton magnetic resonance spectroscopy in acute multiple sclerosis lesions. Brain **117**, 49–58 (1994)
50. R.A. Koopmans, D.K. Li, G. Zhu, P.S. Allen, A. Penn, D.W. Paty, Magnetic resonance spectroscopy of multiple sclerosis: in-vivo detection of myelin breakdown products. Lancet (Letter to the Editor) **341**, 631–632 (1993)
51. W. Roser, G. Hagberg, I. Mader, H. Brunnschweiler, E.W. Radue, J. Seelig, L. Kappos, Proton MRS of gadolinium-enhancing MS plaques and metabolic changes in normal-appearing white matter. Magn. Reson. Med. **33**, 811–817 (1995)
52. K.L. Behar, T. Ogino, Characterization of macromolecule resonances in the 1H NMR spectrum of rat brain. Magn. Reson. Med. **30**, 38–44 (1993)
53. K.L. Behar, D.L. Rothman, D.D. Spencer, O.A. Petroff, Analysis of macromolecule resonances in 1H NMR spectra of human brain. Magn. Reson. Med. **32**, 294–302 (1994)
54. I. Mader, U. Seeger, R. Weissert, U. Close, T. Nagele, A. Melms, W. Grodd, Proton MR spectroscopy with metabolite-nulling reveals elevated macromolecules in acute multiple sclerosis. Brain **124**, 953–961 (2001)
55. U. Seeger, I. Mader, T. Nagele, W. Grodd, O. Lutz, U. Klose, Reliable detection of macromolecules in single-volume 1H NMR Spectra of the human brain. Magn. Res. Med. **45**, 948–954 (2001)